Meteorological Reanalyses for the Study of Gulf War Illnesses: Khamisiyah Case Study

D. L. WESTPHAL, T. R. HOLT, S. W. CHANG, N. L. BAKER, T. F. HOGAN, L. R. BRODY, R. A. GODFREY, AND J. S. GOERSS

Naval Research Laboratory, Monterey, California

J. A. CUMMINGS, D. J. LAWS, AND C. W. HINES

Fleet Numerical Meteorology and Oceanography Center, Monterey, California

(Manuscript received 1 February 1998, in final form 23 September 1998)

ABSTRACT

The Marine Meteorology Division of the Naval Research Laboratory (NRL), assisted by the Fleet Numerical Meteorology and Oceanography Center, has performed global and mesoscale reanalyses to support the study of Gulf War illness. Realistic and quantitatively accurate atmospheric conditions are needed to drive dispersion models that can predict the transport and dispersion of chemical agents that may have affected U.S. and other coalition troops in the hours and days following the demolition of chemical weapons at Khamisiyah, Iraq, at approximately 1315 UTC 10 March 1991. The reanalysis was conducted with the navy's global and mesoscale analysis and prediction systems: the Navy Operational Global Atmospheric Prediction System and the NRL Coupled Ocean–Atmosphere Mesoscale Prediction System. A comprehensive set of observations has been collected and used in the reanalysis, including unclassified and declassified surface reports, ship and buoy reports, observations from pibal and rawinsonde, and retrievals from civilian and military satellites. The atmospheric conditions for the entire globe have been reconstructed using the global system at the effective spatial resolution of 0.75°. The atmospheric conditions over southern Iraq, Kuwait, and northern Saudi Arabia have been reconstructed using the mesoscale system at the spatial resolutions of 45, 15, and 5 km. In addition to a baseline reanalysis, perturbation analyses were also performed to estimate the atmospheric sensitivity to observational error and analysis error. The results suggest that the reanalysis has bounded the variability and that the actual atmospheric conditions were unlikely to differ significantly from the reanalysis.

The synoptic conditions at and after the time of the detonation were typical of the transitional period after a Shamal and controlled by eastward-propagating small-amplitude troughs and ridges. On the mesoscale, the conditions over the Tigris–Euphrates Valley were further modulated by the diurnal variation in the local circulations between land, the Persian Gulf, and the Zagros Mountains. The boundary layer winds at Khamisiyah were from NNW at the time of the detonation and shifted to WNW in the nocturnal boundary layer. On the second day, a strong high passed north of Khamisiyah and the winds strengthened and turned to the ESE. During the third day, the region was dominated by the approach and passage of a low pressure system and the associated front with the SE winds veering to NW.

A transport model for passive scalars was used to illustrate the sensitivity to the reanalyzed fields of potential areas of contamination. Transport calculations based on various release scenario and reanalyzed meteorological conditions suggest that the mean path of the released chemical agents was southward from Khamisiyah initially, turning westward, and eventually northwestward during the 72-h period after the demolition. Precipitation amounts in the study area were negligible and unlikely to have an effect on the nerve agent.

1. Introduction

In March 1991 after the ground campaign of Operation Desert Storm, U.S. Army demolition teams destroyed ammunition bunkers and stacks of munitions at the Khamisiyah Ammunition Storage Area in southeastern Iraq (Fig. 1). The U.S. government now believes that the 122-mm rockets destroyed at 1315 UTC 10 March 1991 in an excavated area known as ''the Pit'' were filled with chemical agents sarin and cyclosarin. It has been suggested that low-level exposure to these chemical agents, commonly known as nerve gas, could have led to the symptoms associated with Gulf War Syndrome or Gulf War Illnesses. Ongoing investigative studies of this possibility require accurate atmospheric transport and dispersion modeling in order to assess the concentration of the gas relative to troop positions. This in turn requires an analysis of the complicated, time-

Corresponding author address: Dr. Simon W. Chang, Naval Research Laboratory, 7 Grace Hopper Street, Stop 2, Monterey, CA 94943.
E-mail: simon.chang@nrl.navy.mil

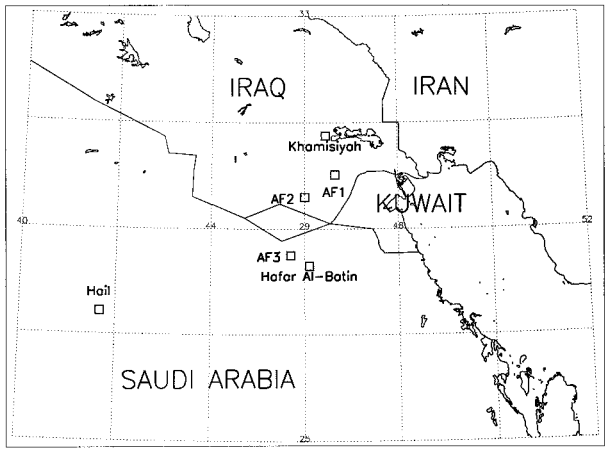

FIG. 1. Map of the Kuwait and Iraq regions showing locations of references sites. The symbols AF1, AF2, and AF3 denote the locations of the mobile USAF meteorological stations referred to in Figs. 16 and 17.

dependent mesoscale structure of the atmosphere at frequent intervals. The analysis must be carried out for several days since the release may have continued for 36 or more hours after the initial detonation and since even low concentrations of nerve agent far from Khamisiyah are of interest to epidemiologists.

Archived operational global analyses during the Gulf War from the Navy Fleet Numerical Meteorology and Oceanography Center (FNMOC), the National Centers for Environmental Prediction (NCEP), and the European Centre for Medium-Range Weather Forecasts (ECMWF) provide some estimate of the atmospheric condition. The region is relatively data sparse in the best of times and, with the absence of Iraqi observations, was particularly poorly observed during the Gulf War. In addition, these archived global analyses have insufficient horizontal resolution (1°–2°), vertical resolution (~10 levels in the troposphere), and temporal resolution (6 or 12 h) to describe the mesoscale structure. Furthermore, the civilian operational analyses did not have access to data that came over classified networks, including the winds from Saudi Arabian rawinsondes, and the classified navy ship, rawinsonde, and surface reports.

The meteorological conditions can be reconstructed by using a single archived analysis at the initial (detonation or earlier) time to initialize an extended (3–5 day) simulation of the period of interest. This method is not practical because it ignores valuable data during the course of the simulation and the model will likely drift from the observed state over the forecast period.

The best reconstruction, called reanalysis, solves these problems and meets the requirements of the epidemiological study. In reanalysis, the present-day data assimilation and prediction systems are applied to the historical data to produce the best possible analysis for three reasons. 1) Significant improvements have been made to data assimilation methods since 1991. Improved, more comprehensive, quality control procedures are available and more data types are now processed. 2) The datasets are more complete because the operational data-cutoff constraint has been removed. 3) The associated numerical weather prediction models are run at higher resolution and have more complete physical parameterizations. The resulting reanalysis is generally accepted as the most accurate analysis possible with the highest resolution allowed by the available resources. While the reanalysis is done every 6 or 12 h, the forecast models provide the data for the interim periods as often as is desired.

This report describes the application of the reanalysis approach to a study of the meteorological conditions for the time and location of the destruction of chemical weapons at the Khamisiyah munitions depot in support of the study of Gulf War Illness. This reanalysis utilizes the Naval Research Laboratory's (NRL) global and mesoscale data assimilation and prediction systems with the most complete set of observations available for the period to produce the most realistic atmospheric conditions possible. The data assimilation and prediction systems are made up of a complex quality control for observations, multivariate optimum interpolation analysis, a global weather prediction model, and a mesoscale prediction model. The global reanalysis determines the large synoptic-scale circulation during March 1991 and provides detailed boundary conditions, at a resolution of approximately 80 km, for the mesoscale reanalysis. The mesoscale reanalysis defines the mesoscale circulation and evolution of the planetary boundary layer structure, which control the dispersion of the nerve agent.

In addition to a baseline reanalysis, several data-denial and observation perturbation reanalyses were carried out to set a bound on the meteorological variability due to possible observational and analysis errors. A simple transport model, driven by mesoscale wind fields, is used to illustrate the importance of differences in the various reanalyses to nerve agent transport.

The methodology and preliminary results of the reanalysis were reviewed and approved by two outside expert panels convened by the Department of Defense. The reanalyzed meteorological fields have been supplied to transport and dispersion (T&D) modelers at the Naval Surface Warfare Center at Dahlgren, Virginia, and the Defense Special Weapons Agency at Alexandria, Virginia, for detailed nerve gas concentration and dosage calculations. The final epidemiology findings based on these dosage calculations and troop locations during the Gulf War compiled by the U.S. Army Center for Health Promotion and Preventive Medicine were reported to the Presidential Advisory Committee on Gulf War Illnesses on 29 July 1997 by the Office of Special Assistant to the Deputy Secretary of Defense for the Gulf War Illnesses (OSAGWI).

This report documents the data assimilation and prediction systems, the reanalyses, and the transport cal-

culations. In section 2, the global and mesoscale data assimilation and prediction systems and observations are discussed. In section 3, the reanalyzed synoptic and mesoscale meteorological conditions during 10–13 March 1991 at the Khamisiyah site are discussed and compared with available observations. The methodology and results of the data-denial and perturbed observation analyses are discussed in section 4. The results of the transport model are presented in section 5. Finally, a summary is given in section 6. In the remainder of this report all dates will refer to the year 1991.

2. The reanalysis procedure

The navy's operational atmospheric data assimilation and prediction systems are designed to fulfill the Department of Defense requirement of supporting simultaneously at least two regional conflicts. This need has been satisfied since 1982 by running an operational global prediction system for global data assimilation and prediction, and multiple relocatable operational regional or mesoscale limited-area models that cover the regions of interest. Currently, the Navy Operational Global Atmospheric Prediction System (NOGAPS) is running at FNMOC twice daily, producing 5- and 10-day global predictions with a 6-h data assimilation cycle. NOGAPS atmospheric analyses and predictions have been used to drive a suite of ocean prediction systems and regional atmospheric prediction systems. At present a nonhydrostatic system, the Coupled Ocean–Atmosphere Mesoscale Prediction System (COAMPS), is running twice a day over four regions routinely and producing 48-h regional predictions with a 12-h data assimilation cycle. To re-create the atmospheric conditions to support a detailed transport and dispersion of the nerve agent from Khamisiyah munitions depot, a reanalysis with both the global and the mesoscale systems, NOGAPS and COAMPS, is carried out.

The reanalysis approach employs analysis and prediction systems to perform data assimilation of historical observations, thus obtaining the most realistic atmospheric conditions for some period in the past. The reanalysis typically starts from climatology or an archived analysis of coarse spatial resolution and proceeds forward one data assimilation cycle at a time. These cycles consist of a short-range forecast by the prediction model, which produces the first-guess fields for the analysis, and the objective analysis with observations. Most reanalyses are done for climate and atmospheric predictability research and, therefore, are conducted at coarse spatial resolutions suitable for global-scale applications or climate studies. These include the NASA reanalysis for 1985–90 (Schubert et al. 1993), the ECMWF reanalysis for 1979–94 (Gibson et al. 1996), and the NCEP reanalysis for 1957–96 (Kalnay et al. 1996).

A description of NOGAPS can be found in Rosmond (1992), Hogan and Rosmond (1991), and Hogan and Brody (1993). NOGAPS is a global spectral model with 159 triangular harmonic truncation (T159) and 18 vertical layers (L18) in a σ-p vertical coordinate. The physical parameterizations of the NOGAPS prediction model include gravity wave drag (Palmer et al. 1986), a relaxed Arakawa–Schubert convective parameterization (Arakawa and Schubert 1974), gridscale precipitation (Haltiner and Williams 1980), shallow convection (Tiedtke 1984), planetary boundary layer (Louis et al. 1982), short- and longwave radiation (Harshvardhan et al. 1987), and a surface energy budget.

Data quality control (QC) and the multivariate optimum interpolation analysis (MVOI) are the major components of the data assimilation system of NOGAPS. The quality control of the observations in the global database at FNMOC includes checking for gross errors and for internal consistency (Baker 1992). The complex quality control (CQC) of rawinsondes developed at NCEP is part of the QC suite (Baker 1994). In the data assimilation cycle of NOGAPS, 6-h NOGAPS forecasts provide the background field (first guess). The MVOI technique utilizes observed data to compute increments to the background fields in such a way that the mean squared error of the analysis will be minimized statistically (Barker 1992; Goerss and Phoebus 1992). Additional QC is performed within the MVOI to ensure consistency with the background fields and with other observations.

The atmospheric component of COAMPS (Hodur 1997) with nonhydrostatic dynamics is used for the mesoscale analysis and prediction. The triply nested grids of COAMPS are centered around Kuwait and have horizontal resolutions of 45, 15 and 5 km over the outer, middle, and inner domains, respectively, and 30 vertical levels with the highest vertical resolution in the planetary boundary layer, with the first few levels at 10, 25, 55 m, etc. As it will be shown, the released nerve gas was quickly transported out of the 5-km grid 12 h after the detonation. The 5-km grid is, nevertheless, valuable to resolve the detailed atmospheric structure near the source for T&D models. Figure 2 shows the reanalysis domains of the three COAMPS grids. For the two outer grids, the Kain–Fritsch cumulus parameterization is employed (Kain and Fritsch 1993), while explicit cloud physics (Rutledge and Hobbs 1983) is used in the innermost grid and for stratiform precipitation in the outer grids. The planetary boundary layer is parameterized based on the turbulent kinetic energy equation and the mixing length. Monin–Obukhov similarity is used for the surface layer (Louis et al. 1982). Parameterizations for the atmospheric radiative transfer and soil physics are similar to those in NOGAPS. Operationally, COAMPS uses the NOGAPS forecast fields for its lateral boundary conditions on the outer mesh utilizing the Davies (1976) method. In this reanalysis, COAMPS uses the NOGAPS reanalyzed fields as the lateral boundary values. The data assimilation for COAMPS is similar to that in NOGAPS. In data-sparse regions of the outer grid, selected points from

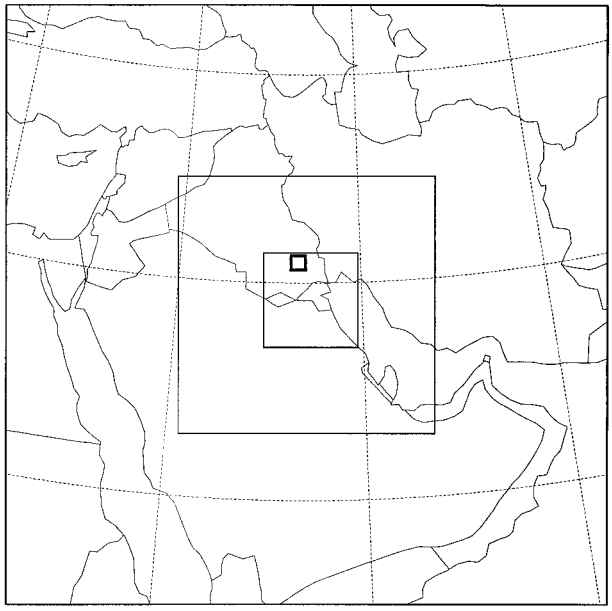

FIG. 2. A map showing the COAMPS domain for the coarse (45 km), medium (15 km), and fine (5 km) grids.

NOGAPS-analyzed fields are automatically inserted as synthetic observations to reduce any possible model drift.

The FNMOC global datasets of terrain height, surface albedo, climatological deep soil temperature, climatological ground wetness, and surface roughness are used by both NOGAPS and COAMPS after interpolation to their respective model grids. Soil temperature and ground wetness are predicted variables in both models. The spatial resolution of these parameters is approximately 1° longitude and latitude, except for terrain, which originates from a master dataset with a 100-m resolution. The sea surface temperature (SST) reanalyses were performed every 12 h directly on the NOGAPS global and the COAMPS triply nested computational grids using the COAMPS Ocean Data Assimilation system. The SST reanalyses were started from the NCEP 1° resolution, monthly SST climatology (Reynolds and Smith 1994) interpolated in time and space to the NOGAPS and COAMPS model grids. The satellite-derived SST observations came from the National Oceanic and Atmospheric Administration–National Aeronautics and Space Administration Advanced Very High Resolution Radiometer (NOAA–NASA AVHRR) Oceans Pathfinder datasets for the time period of the reanalysis. The Pathfinder datasets used were the 9-km day–night SST retrievals of the highest quality. The SST reanalyses also used in situ observations from ships, buoys, and expendable bathythermographs, but the primary source of observational data was the Pathfinder datasets.

One of the primary advantages that FNMOC has over civilian meteorological centers (such as NCEP) is the capability to include classified observations in its routine analysis and forecast systems. This proved to be very important during Desert Storm. Saudi Arabia normally transmits their rawinsonde observations over the unclassified Global Telecommunications Systems (GTS); these observations are then available worldwide shortly thereafter. Because of concerns that Iraq might use chemical weapons, and would use the Saudi Arabian rawinsondes to assist their decisions as to when to deploy the weapons, Saudi Arabia withheld the wind rawinsonde observations from the GTS. Consequently, it was arranged that the Saudi rawinsondes would be transmitted over the confidential communications circuits. This allowed FNMOC to use these important observations in real time during Desert Storm.

The observations used in the reanalysis are 1) surface observations—unclassified and declassified surface observations, fixed and drifting buoys, civilian ship reports, declassified navy ship reports, and Australian sea level pressure bogus; 2) upper-air observations—pilot balloon observations, unclassified and declassified rawinsonde observations, and aircraft reports; and 3) satellite retrievals—temperature soundings from NOAA and Defense Meteorological Satellite Program (DMSP) satellites, and cloud-track winds from geostationary satellites. Figure 3 shows the locations of the various observation types mentioned above that fall within the ± 3 h window and used in the NOGAPS reanalysis at 1200 UTC 10 March.

The primary differences between the operational dataset and the one used in the reanalysis are as follows. The reanalysis includes observations that arrived at FNMOC later than the cutoff time (3.5 h) for the operational forecast run. Conversely, a small number of secret observations were used operationally, but have not been declassified and were not used in the reanalysis. Finally, Special Sensor Microwave/Imager (SSM/I) marine wind speeds became operational in September of 1990, but were not archived until May 1991, and therefore were not used in the reanalysis. In spite of the absence of these two types of observations, the global reanalysis is superior than the operational analysis due to the improved data assimilation and numerical model as indicated by the current and historical analysis errors.

To reduce imbalances in the initial state and to spin-up the boundary layer and moisture distribution, the NOGAPS reanalysis began at 0000 UTC 28 February, or more than 10 days (40 data assimilation cycles) before the detonation, using the archived operational analysis for 28 February. For the same reason, the COAMPS reanalysis began with the reanalyzed NOGAPS fields valid at 1200 UTC 8 March, or 2.5 days (five data assimilation cycles) before the detonation. Both the NOGAPS and COAMPS reanalyses were terminated at 1200 UTC 15 March.

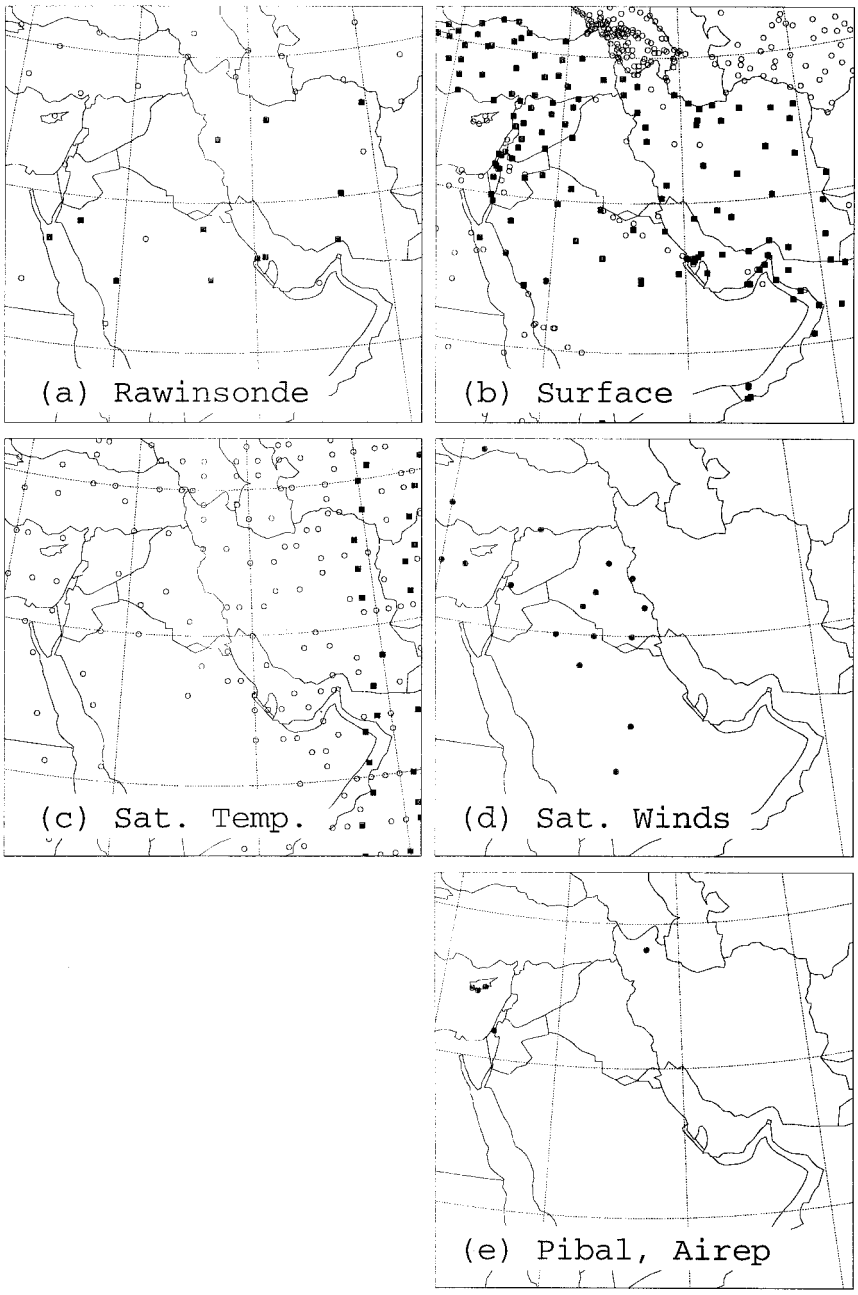

FIG. 3. Locations of observations within the window of ±3 h of the reanalysis valid 1200 UTC 10 March: (a) rawinsonde, (b) surface observations, (c) satellite temperature retrievals, (d) satellite cloud-track winds, and (e) aircraft reports. Closed symbols in (a) and (b) represent data available only through classified networks to military sites during the Gulf War. Open and closed symbols in (c) represent NOAA and DMSP data, respectively. In (e) the single observation in northern Iran is an aircraft report; the four other observations are pibals.

3. The reanalyzed meteorological conditions

A description of the synoptic- and mesoscale meteorological conditions within several days of the destruction of the Khamisiyah munitions depot, as depicted in the NOGAPS and COAMPS reanalyses, is given in this section. First, the NOGAPS large- and regional-scale circulations for 8–14 March are described with an emphasis on the 500- and 1000-hPa levels. Then, the COAMPS analyses on the 45- and 15-km meshes are discussed, including comparisons with surface observations and rawinsonde data.

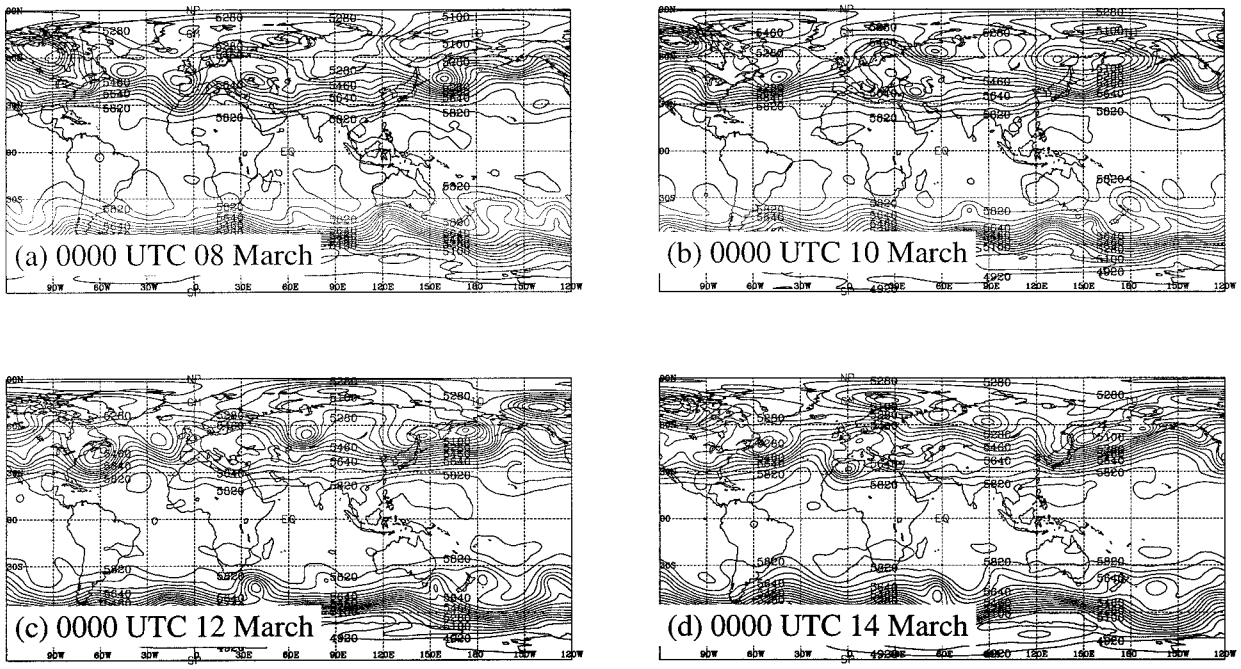

FIG. 4. NOGAPS baseline reanalysis of 500-hPa geopotential heights (m, contoured every 60 m) for 0000 UTC 8 March–14 March at 2-day intervals.

a. Large-scale condition

In the days previous to the detonation at Khamisiyah, the 500-hPa level showed a split in the westerlies extending from western Europe to the Caspian Sea (Fig. 4). The northern branch of the westerlies extended from Scandinavia through northern Russia while the southern branch extended from near the Strait of Gibraltar eastward across the Mediterranean and North Africa into the Middle East. Since the Khamisiyah area was under the influence of the southern branch, only synoptic-scale features moving through it would be expected to affect the region. A description of the movement of these features follows.

On 8 March, strong 500-hPa troughs were located southward from Spain into northwest Africa and from the eastern shores of the Mediterranean into Iran (Fig. 4a). A marked ridge through the central Mediterranean separated these troughs. Two days later, on 10 March, the trough over Spain had moved steadily eastward to the central Mediterranean while the eastern trough showed little movement (Fig. 4b). The ridge separating these two troughs weakened and progressed slowly to western Turkey. On 12 March, the western trough moved into the eastern Mediterranean and northern Egypt with flow east of this trough quite zonal over the Khamisiyah area (Fig. 4c). By 14 March, the trough had progressed covering most of the Middle East, while a new trough in the southern branch of the westerlies was found over northwest Africa (Fig. 4d).

b. Regional condition

On a regional scale the weather over the Khamisiyah area can be divided into the periods before and after 1200 UTC 10 March. Before this date, synoptic conditions were controlled by an upper-level low embedded in the eastern trough described above. Afterward, the synoptic conditions became increasingly under the influence of both the western upper-level trough and the ridge building ahead of it.

On 8 March, the upper-level low was located over the Sea of Azov with general west-northwesterly flow over Iraq and the northern Persian Gulf (Fig. 5a). At the surface level, a trough of low pressure was found over Turkey with high pressure covering most of Saudi Arabia and Iraq (Fig. 6a). Winds at the 1000-hPa level were mainly northeasterly over southern Iraq while northwesterlies blew over the Persian Gulf in association with a Shamal in this region.

By 9 March, the upper-level low had moved southeastward to the eastern tip of the Black Sea (Fig. 5b). A surface low developed over extreme northern Iraq in association with the upper low (Fig. 6b). High pressure still covered most of southern and central Saudi Arabia. The 1000-hPa winds shifted to southeasterly over most of eastern Iraq ahead of the surface low. With high pressure still over Saudi Arabia, northwesterlies covered the Persian Gulf.

The upper-level low continued to move eastward so that by 10 March it was located near extreme southeastern Turkey (Fig. 5c). The associated surface low

moved to northern Iraq, allowing the 1000-hPa winds to shift northwesterly over most of Iraq with southeasterlies only over the northern Persian Gulf (Fig. 6c).

At 1200 UTC 10 March (just before the release event), the 500-hPa low that had been moving southeastward for the past two days, turned eastward and began accelerating eastward through northern Iran to the Caspian Sea (Fig. 5d). As this feature moved out, the upper-level flow over the Khamisiyah region turned westerly. At the surface, the low accelerated eastward across Iran (Fig. 6d) and high pressure rebuilt over Iraq with the 1000-hPa winds turning to northerly to northwesterly over southern Iraq and the northern Persian Gulf. Only minor changes occurred over the Khamisiyah region during the next 24 h.

Twenty-four hours later at 1200 UTC 11 March, a flat ridge as seen at the 500-hPa level developed over Iraq and northern Saudi Arabia (Fig. 5e). At the surface, high pressure continued to build over northern Iraq and northern Iran (Fig. 6e). The 1000-hPa winds were generally northeasterly over most of southern Iraq, but north to northwesterly over the Persian Gulf. Noteworthy is a surface trough that began to develop over the Red Sea with 1000-hPa southerly winds over most of western Saudi Arabia.

By 12 March, significant changes were occurring at both the 500-hPa and surface levels. The large-scale upper trough moving eastward across the Mediterranean was now over the eastern Mediterranean (Fig. 5f). The ridge ahead of this trough continued to amplify as it moved eastward over the Khamisiyah region. A shallow surface low developed in the previously mentioned trough and now was located in central Saudi Arabia (Fig. 6f). Between this low and strong high pressure over Iran, the 1000-hPa winds shifted to southeasterly over Iraq and eastern Saudi Arabia. Winds over the northern part of the Persian Gulf became light and variable.

By 13 March, the large-scale 500-hPa trough had moved from the Mediterranean to Syria and western Iraq (Fig. 5g). The ridge out ahead of this trough continued to amplify as it moved eastward over Iran. The surface low over central Saudi Arabia moved northeastward to southern Iraq (Fig. 6g). The 1000-hPa winds over most of the Persian Gulf and extreme southeast Iraq were southeasterly ahead of the low. However, over western Iraq (behind the low), the winds shifted northwesterly. By 14 March, all of southern Iraq was showing northwesterly winds as the surface low moved into Iran.

c. Mesoscale condition

Because the 5-km grid is too small to depict typical meteorological patterns and the COAMPS 5-km analyses are comparable to those on the 15-km grid, COAMPS 15-km analyses are discussed for the period 1200 UTC 10 March through 1200 UTC 13 March. The mesoscale flow in the Khamisiyah area just before the demolition (Fig. 7a) shows the same features as those seen in the larger-scale NOGAPS analysis (Fig. 6d), such as NNW low-level flow down the Tigris–Euphrates Valley on the back side of the broad surface low in Iran. Surface winds were strong over the Persian Gulf (6–10 m s^{-1}). Visible satellite imagery indicated clear condition over the Khamisiyah region with only scattered clouds south of 25°N (Fig. 8a). The COAMPS cloud forecasts shows more clouds in the Khamisiyah area and to the northeast over Iran than observed in satellite imagery, but the COAMPS forecast clouds are generally scattered (Fig. 8b).

At 1200 UTC 11 March, the COAMPS forecasts indicate the low-level flow in the Khamisiyah area and just to the south shifted to NE (Fig. 7b) as the low pressure region over Iran weakened and moved eastward and the surface trough developed over the Red Sea. The satellite image (Fig. 9a) shows continuing clear conditions over the Khamisiyah region with more organized east–west-aligned cloud activity still located south of 25°N. COAMPS cloud forecasts show general agreement with satellite observations, indicating clear skies over Khamisiyah while also depicting organized clouds south of 25°N with the correct alignment (Fig. 9b).

At 1200 UTC 12 March, the shallow surface low southwest of Khamisiyah and the strong high pressure over northern Iran (Fig. 6f) were the prominent low-level features in the region. As a result, the low-level pressure gradient tightened over the Khamisiyah region, causing the surface winds to increase to 6–7 m s^{-1} and shift to ESE (Fig. 7c). The satellite image also reveals the approaching low pressure region (Fig. 5f) with increased clouds over the Saudi peninsula (Fig. 10a). The COAMPS cloud forecast (Fig 10b) again shows good agreement with observations.

By 1200 UTC 13 March, the surface low moved northeastward to southern Iraq and was the prominent low-level feature in the region (Fig. 6g). The COAMPS low-level flow shows weak cyclonic circulation in association with the surface low with generally NNE flow (4–5 m s^{-1}) at Khamisiyah, shifting cyclonically to southerly south of Khamisiyah (Fig. 7d). Strong SE winds of 6–10 m s^{-1} were present over the Persian Gulf. Abundant cloud coverage was evident over Kuwait and southern Iraq as well as over the Saudi peninsula (Fig. 11a). COAMPS cloud forecasts also predict substantial cloudiness throughout the region (Fig. 11b). Despite the general trend of increasing cloudiness over the 3-day period, the modeled accumulated precipitation in the study exceeded 5 mm in only a few locations with heavy amounts in the mountains north of the Tigris–Euphrates Valley (Fig. 12).

The two rawinsonde stations closest to Khamisiyah (Fig. 3a) fortuitously lie near the path of gas transport (see section 5) and thus are particularly valuable in validating the COAMPS analyses and forecasts for the Khamisiyah region. Hafar al Batin (28.33°N, 46.12°E; Fig. 1) is located approximately 250 km south of Kham-

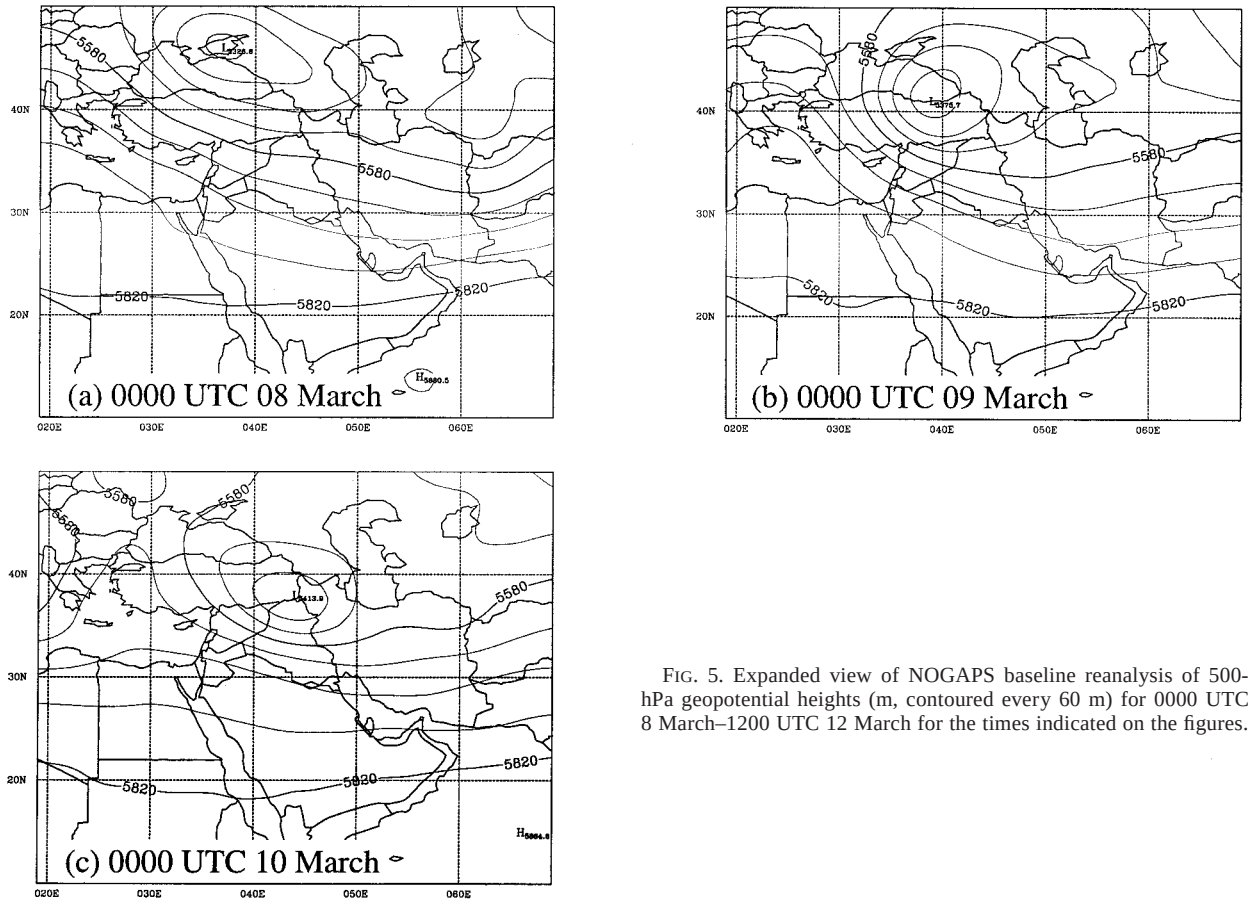

FIG. 5. Expanded view of NOGAPS baseline reanalysis of 500-hPa geopotential heights (m, contoured every 60 m) for 0000 UTC 8 March–1200 UTC 12 March for the times indicated on the figures.

isiyah. Hail (27.43°N, 41.68°E) is located approximately 600 km SSW of Khamisiyah. In the following discussion of the rawinsonde data, comparisons will be made to the COAMPS forecasts at these locations to show short-term variabilities. Hail is located outside of the 5-km grid, so the COAMPS 15-km forecasts will be compared.

The synoptic features described above are apparent in the time–height cross sections of both the rawinsonde data and the COAMPS forecasts (Figs. 13 and 14). Low-level flow at 1200 UTC 10 March at Hafar al Batin is generally NNW throughout the boundary layer (lowest 1.5–2 km) and westerly aloft. Farther west at Hail, the circulation associated with the high pressure region resulted in more easterly low-level flow that turned to westerly near the top of the boundary layer. The development of the nocturnal inversion is shown clearly in the Hafar al Batin observations and COAMPS forecast.

At 1200 UTC 11 March the influence of the surface trough appeared as southerly low-level winds at Hail (Fig. 14a). The COAMPS forecasts capture the observed southerly flow and warming of the deep boundary layer (over 2 km) in advance of the surface trough (Fig 14b). By 1200 UTC 12 March, the southeasterly low-level winds, and the associated warming, reached Hafar al Batin (Fig 13a). The winds were strong (10 m s^{-1}) in response to the tightening pressure gradient over Iraq (Fig. 6f). COAMPS also shows the strongest winds (as discussed earlier) with speeds approximately 10 m s^{-1} (Fig. 13b). The passage of the surface low and upper-level trough after 1200 UTC 12 March is best seen in the sounding at Hail at 0000 UTC 13 March. Both the observed and modeled boundary layer flow turned westerly behind the trough. Not until 1200 UTC 13 March did the boundary layer flow at Hafar al Batin begin to turn westerly.

The COAMPS forecast time–height cross section for Khamisiyah is discussed (Fig. 15) because of its obvious relevance to the study, though there are no rawinsonde data for comparison. The conditions at Khamisiyah closely resembled those at Hafar al Batin (Fig 13). However, the boundary layer was cooler and had a stronger and more persistent capping inversion. The low-level

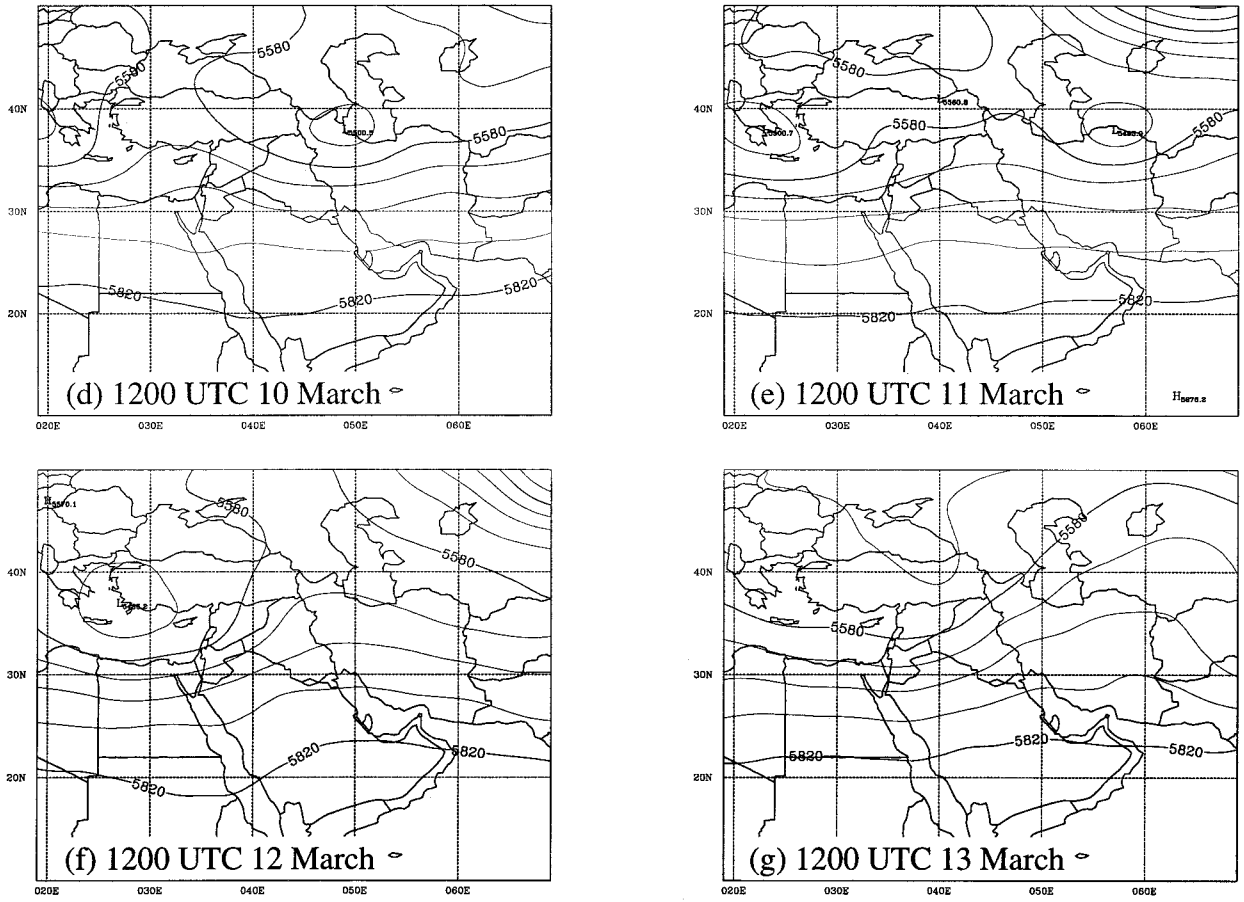

FIG. 5. (*Continued*)

winds followed the same general trends as were seen at Hafar al Batin: initially N, then SE as the low approaches, and lastly NW after the passage of the low.

Observations of the 2-m wind speed and direction were made near Khamisiyah for the time period of 0000 UTC 9 March to 1200 UTC 12 March by mobile U.S. Air Force (USAF) meteorology stations located at 30.02°N, 46.65°E and 29.6°N, 46.0°E (labeled AF1 and AF2 in Fig. 1). The latter station was moved to 28.5°N, 45.7°E (AF3 in Fig. 1) at approximately 1200 UTC 11 March. Like the rawinsonde data, these surface observations are particularly valuable since they were taken 100–175 km SSE of Khamisiyah, along the transport path. These observations were not part of the FNMOC dataset used in the reanalysis. No information is available as to the topographical setting of the mobile stations. Figures 16 and 17 compare the time series of 2-m wind direction and speed at AF1, AF2, and AF3 with the COAMPS 10-m wind forecasts. For the comparison, the forecasted 10-m winds have been reduced to 2-m winds using scaling based on surface layer theory. The observations show N to NW flow in the region for the first 24 h, including the release time (1330 UTC 10 March), supporting earlier discussions of winds in the region. Winds predicted by COAMPS during this period have similar direction but a slightly larger easterly component. The observed winds at both sites decrease from 5 m s^{-1} to near zero during the first 16 h in conjunction with the weakening of the low pressure system over Iran and subsequent weakening of the low-level pressure gradient (Fig. 6e). The modeled winds show a similar weakening at AF1 but not at AF2 (Fig. 16). There the forecasted wind speed is variable, but always less than 6 m s^{-1}. At AF1, the wind increases again to 4 m s^{-1} between 0600 and 1200 UTC 11 March while the forecasted winds remain light.

The mobile unit was relocated to the AF3 location at 1500 UTC 12 March. During the 22 h at this site, the winds shifted from easterly to southerly in association with the shallow low pressure center propagating from the Red Sea (Fig. 6f). Observed wind speeds in the Khamisiyah area reached the largest values of the period (6–8 m s^{-1}) while the pressure gradient was tightening, as discussed above. COAMPS also predicts the wind shift and an increase in wind speeds, though speeds never exceed 6 m s^{-1}. The observations show a 4-h

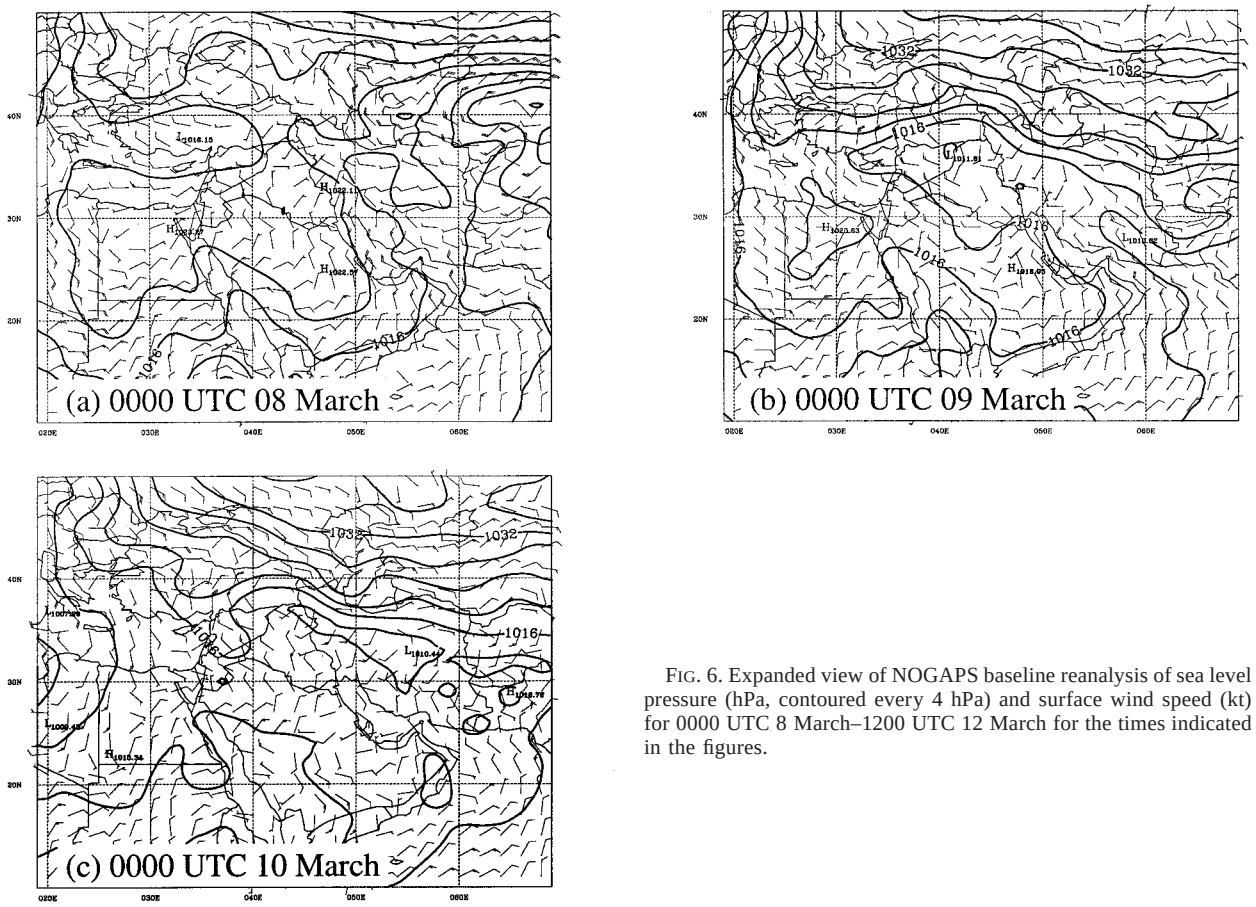

FIG. 6. Expanded view of NOGAPS baseline reanalysis of sea level pressure (hPa, contoured every 4 hPa) and surface wind speed (kt) for 0000 UTC 8 March–1200 UTC 12 March for the times indicated in the figures.

period of weak (<0.5 m s^{-1}) southerly and westerly winds centered around 0000 UTC 12 March.

We conclude that in terms of numerical weather prediction, the forecasted winds would be considered in good agreement with the observations, capturing the wind direction and shifts in wind direction, although there is some disagreement in wind speed. For transport and dispersion calculations, the impact of a wind direction difference of 45° or wind speed difference of 4 m s^{-1} is large. The differences are due to the model characteristics (numerics, physics, etc.), initial and boundary conditions, observational error, and microscale meteorological effects. Unfortunately, there are insufficient data to determine which of these is the cause of the differences. The perturbation transport calculations described in section 5 will shed some light on the impact of these differences on transport of the chemical agents.

4. The alternative reanalyses

The Khamisiyah event occurred in a data-sparse region for mesoscale analysis (e.g., Fig. 3). It is also well established that long-range (greater than 12 h) prediction and analysis from a limited-area model is likely to be dominated by boundary conditions supplied by the global analysis (Errico and Baumhefner 1987). In order to obtain suitable variabilities that potentially could result from errors in observations as well as in the reanalysis, and to assess the stability of the global and mesoscale baseline analyses described above, alternative analyses were carried out. Ideally, sensitivity tests using an adjoint model should be conducted to obtain the most sensitive atmospheric structure, so that maximum perturbation analysis can be acquired to drive the transport and perturbations. At this time, the NRL singular vector technique (Gelaro et al. 1998, manuscript submitted to *Mon. Wea. Rev.*, hereafter GLR) for COAMPS is in development. In its place, an engineering approach has been used for the reanalyses. In this section, the procedure is explained and the alternatively analyzed fields are compared with the baseline analysis fields.

These alternative analyses consist of 1) a COAMPS analysis, referred to as DD15, where all observations within the domain of the COAMPS 15-km grid (Fig. 2)

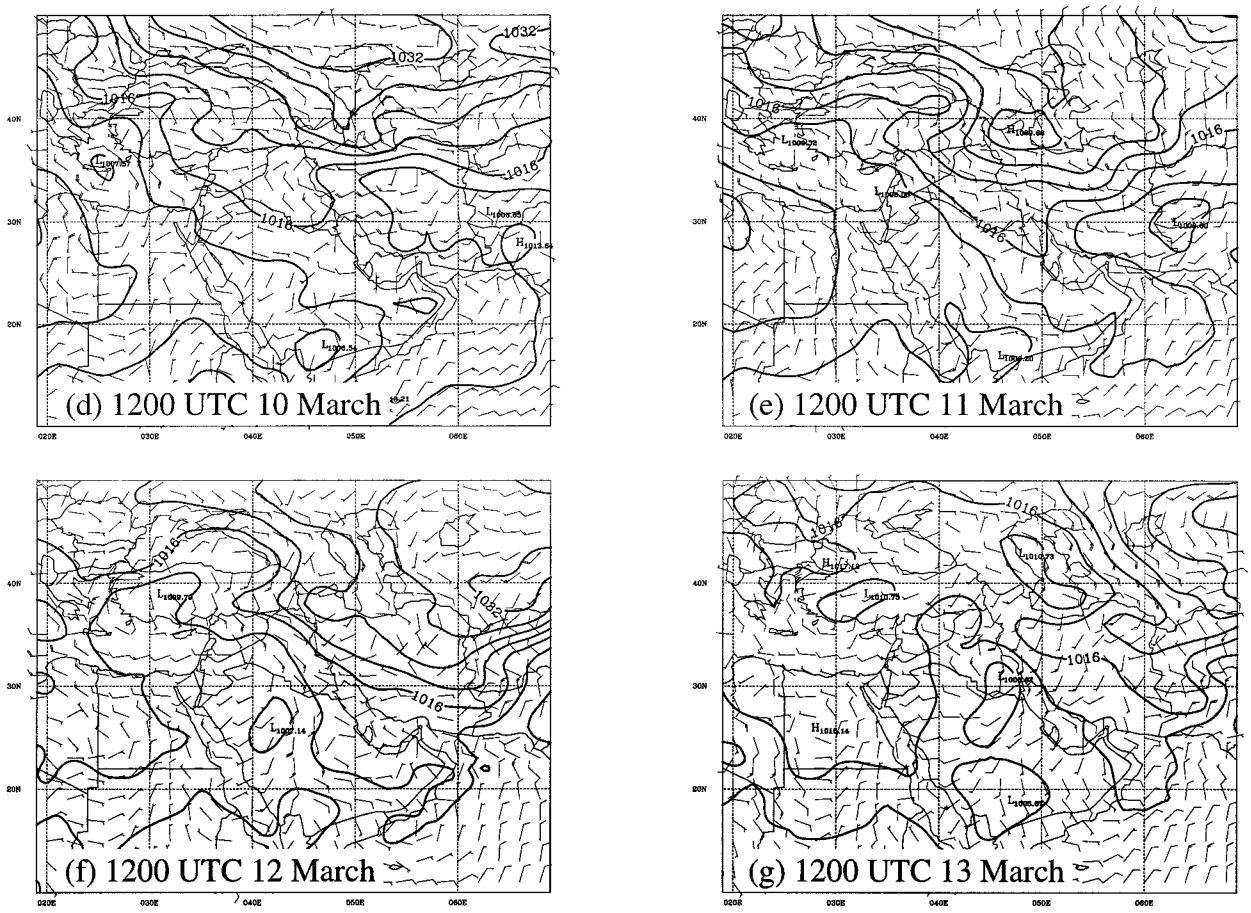

FIG. 6. (*Continued*)

were denied to the data assimilation process; 2) NOGAPS and COAMPS analyses, referred to as DD45, where all observations within the 45-km domain of the COAMPS were denied; an 3) NOGAPS and COAMPS analyses, referred to as RPO, where random, bounded errors were introduced to the global observation database according to the type and altitude of the observation. Table 1 lists all the alternate reanalyses. The COAMPS reanalysis DD45 is the same as a forecast (or hindcast) using boundary conditions from a global analysis in which observations within the mesoscale model domain are not assimilated. The baseline analysis is referred to as BL.

The perturbations introduced to the global observations for the random perturbation of observations (or RPO) reanalyses, are the product of random numbers of $O(1)$ and standard deviations of the observational error for each variable type and source and at different heights. For the errors, the observational-error standard deviations in Goerss and Phoebus (1992) were applied (Table 2). For example, the standard deviation of the observational error of rawinsonde horizontal wind components at the 500-hPa level is 2.8 m s^{-1}, whereas that of the cloud-track wind is 4.8 m s^{-1}. Other standard deviations of observational error not listed in Table 2 used in the perturbed analysis were 10° in wind direction for rawinsonde and pibal surface winds and other surface winds, 20° in wind direction for nonsurface winds, and 2 hPa for surface pressure. The thickness error for satellite retrieval was 1.5 times that of the rawinsonde. For profile observations (e.g., rawinsondes, satellite temperature soundings, and pibals) a random number generator was used to generate a sequence of 16 random numbers between zero and one for the 16 mandatory pressure levels (see Table 2). The sign of the random number for the geopotential height, wind speed, and wind direction at a given level was determined by the evenness or oddness of the fifth, fourth, or third significant digits, respectively. A different random number sequence was used for each reporting station.

Both winds and heights were perturbed for rawinsonde observations. Surface observations of sea level pressure, wind speed, and direction were perturbed; for single-level upper-air observations, both wind speed and wind direction were perturbed. In addition, rawinsonde height perturbations were rounded to the nearest meter

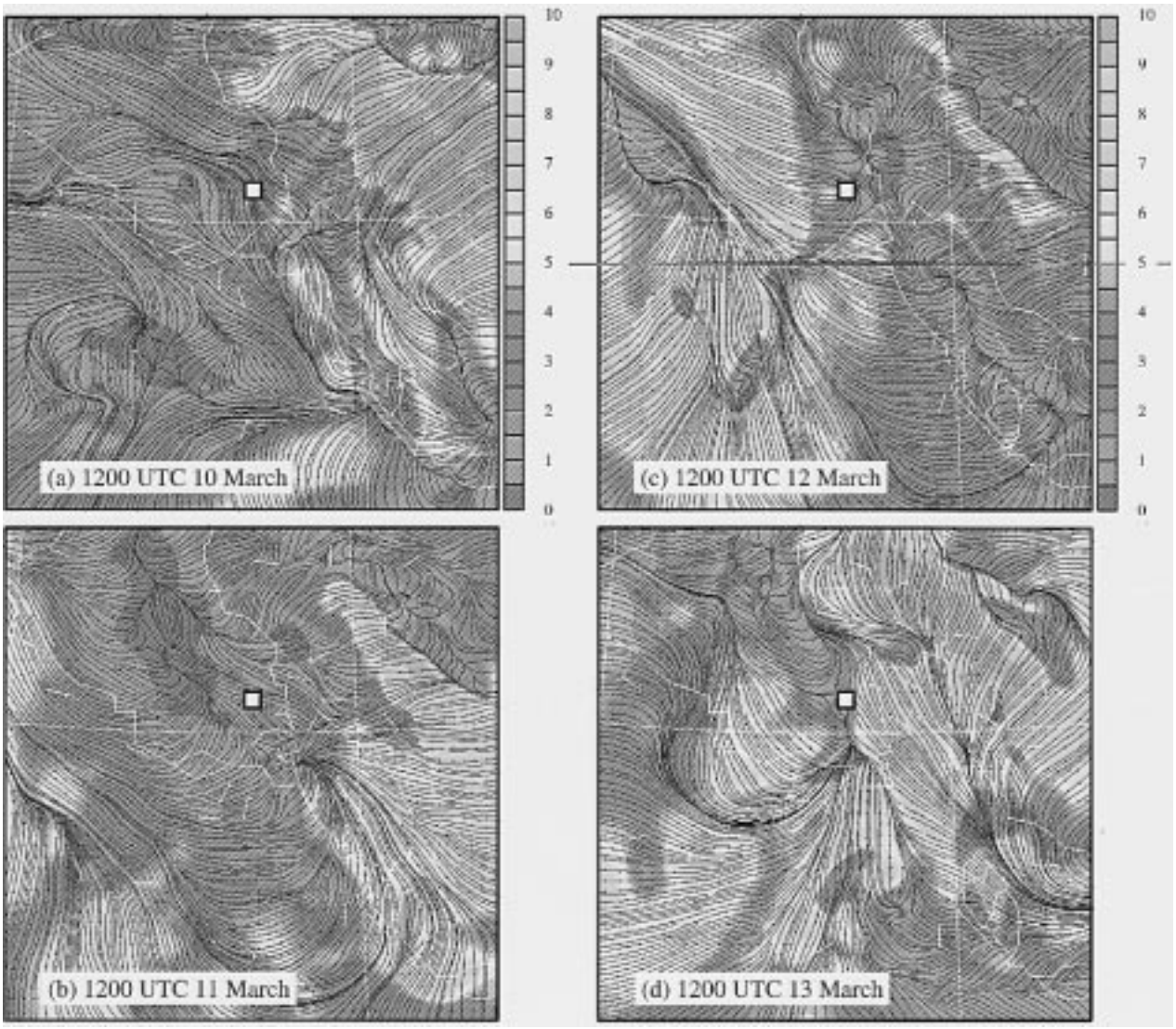

FIG. 7. COAMPS 15-km mesh 12-h forecast of 10-m wind speed (shaded, contour interval of 1 m s^{-1}) and streamlines valid at 1200 UTC for the days indicated. Surface wind observations are plotted in white. Note that in this figure a full barb = 10 m s^{-1}.

for 700 hPa and below, and rounded to the nearest decameter above, to mimic World Meteorological Organization reporting regulations. This was necessary to make the observations compatible with CQC. Since NOGAPS and COAMPS analyses were done in height, the temperature perturbations are consistent with height perturbations. The perturbations were added to the observations prior to the data QC. As a result, the rejection rate for heights in QC doubled from that of the baseline analysis. The overall data rejection rates by QC were slightly higher for the perturbed observations. On several occasions, the random perturbations added to the rawinsonde heights were successfully corrected back to the original observation by the CQC. More often, the small perturbations added to the surrounding data levels prevented CQC from making ''confident corrections,'' and the perturbed observations were accepted.

a. Global baseline (BL) analysis versus data denial (DD45) analysis

In this and the next section, the baseline (BL) analysis is compared with the alternative analyses with a special emphasis over the Persian Gulf region. For most areas outside the Persian Gulf region the differences between the BL analysis and the DD45 analysis (not shown) were small. The only exterior regions with clear differences are the high terrain regions of Greenland, the Himalayas, and Antarctica, where surface pressure differences of several hectopascals were evident and 500-hPa height differences were as large as 20 m. Away from the steep terrain regions and the Persian Gulf, the 500-hPa height root-mean-square (rms) differences are of order 2.5 m, well within the observational error at this level (Table 2), and the surface pressure differences are less than 1 hPa.

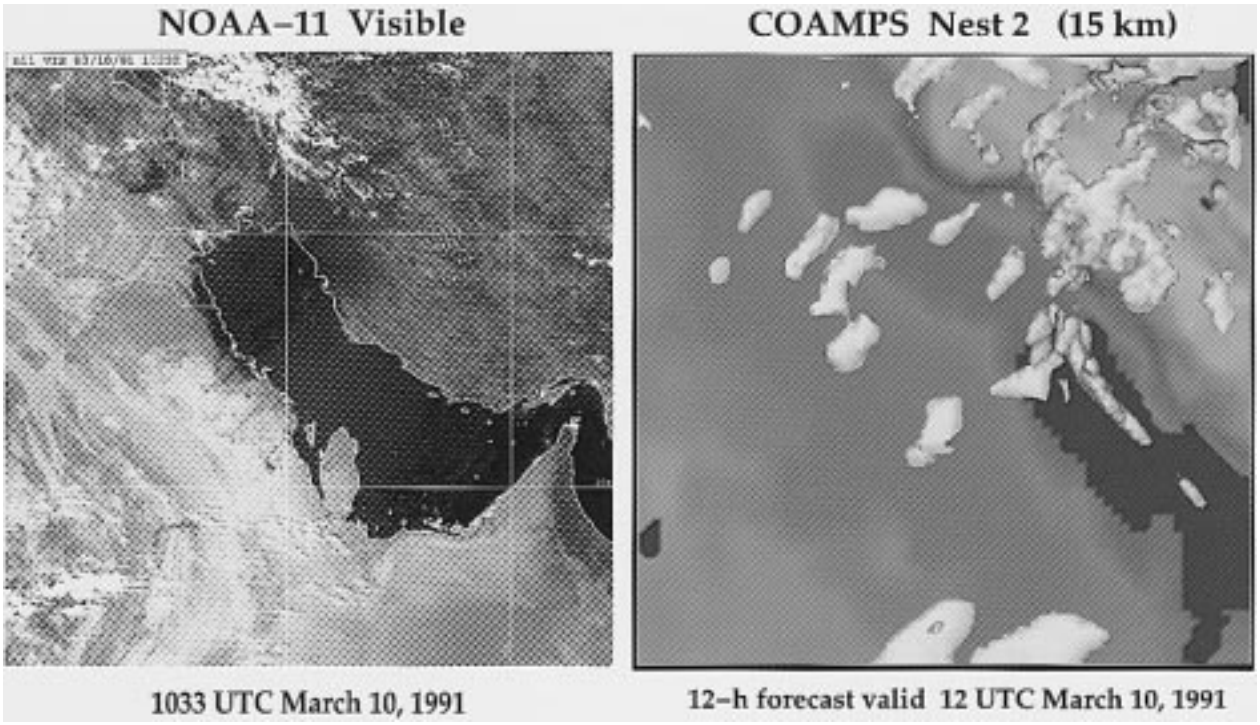

FIG. 8. (a) *NOAA-11* visible satellite image valid at 1033 UTC 10 March and (b) COAMPS 12-h cloud forecast valid at 12 UTC 10 March on the 15-km mesh. The forecast clouds are outlined by contours of cloud liquid or ice content of 0.01 g kg^{-1}. The grayscale depicts cloud temperatures, with whiter shade denoting lower temperatures (higher altitudes).

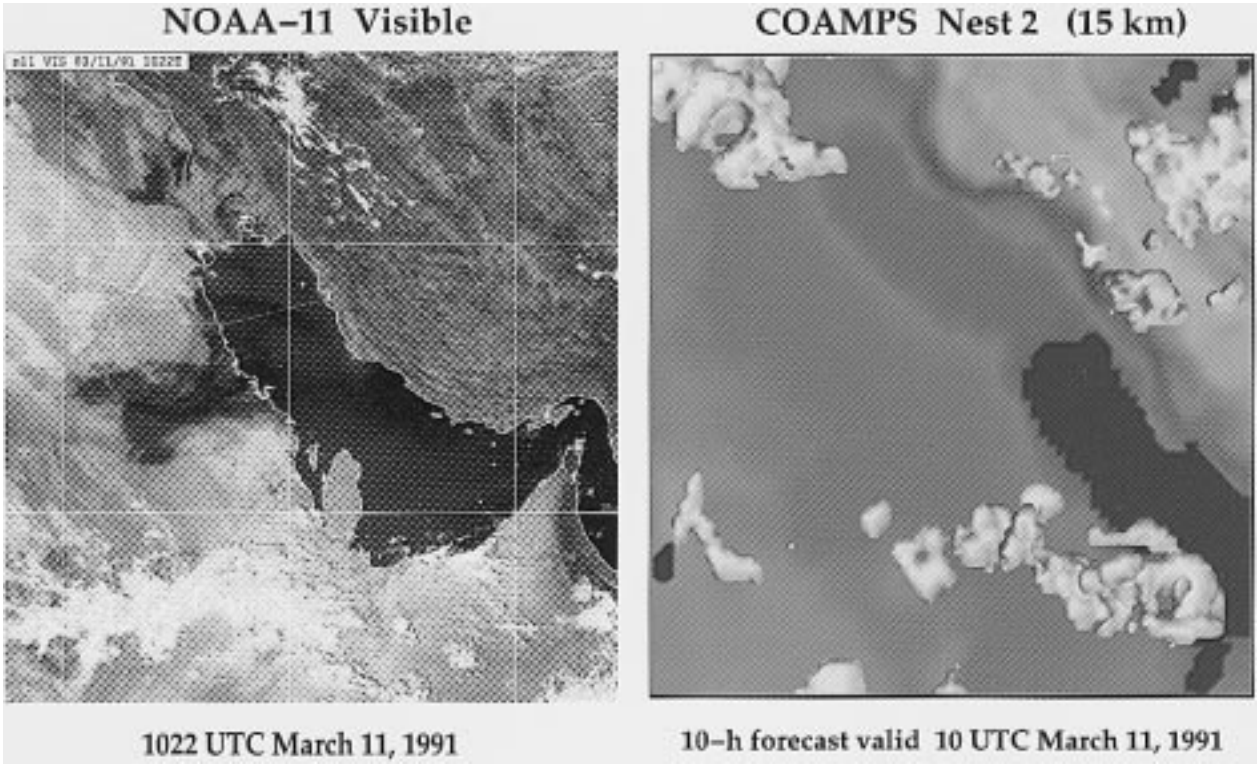

FIG. 9. As in Fig. 8 but (a) for 1022 UTC 11 March and (b) for 1000 UTC 11 March.

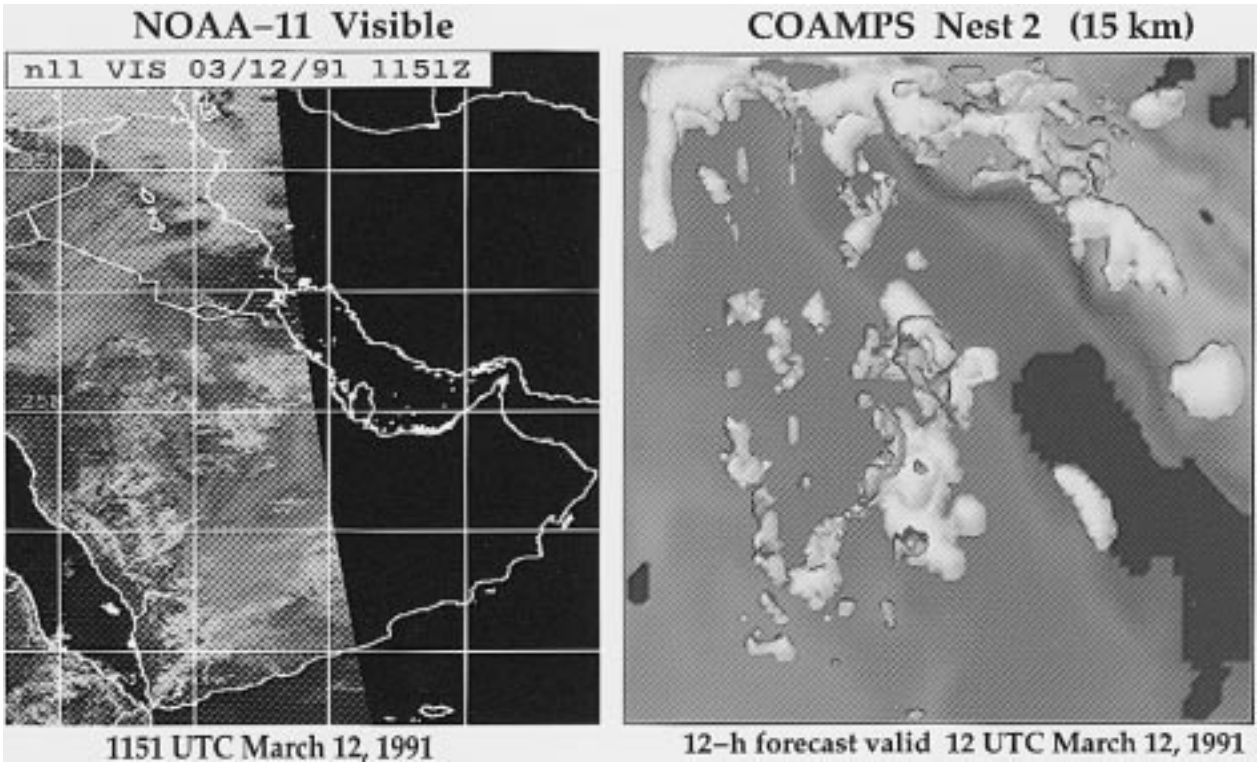

FIG. 10. As in Fig. 8 but (a) for 1151 UTC 12 March and (b) for 1200 UTC 12 March.

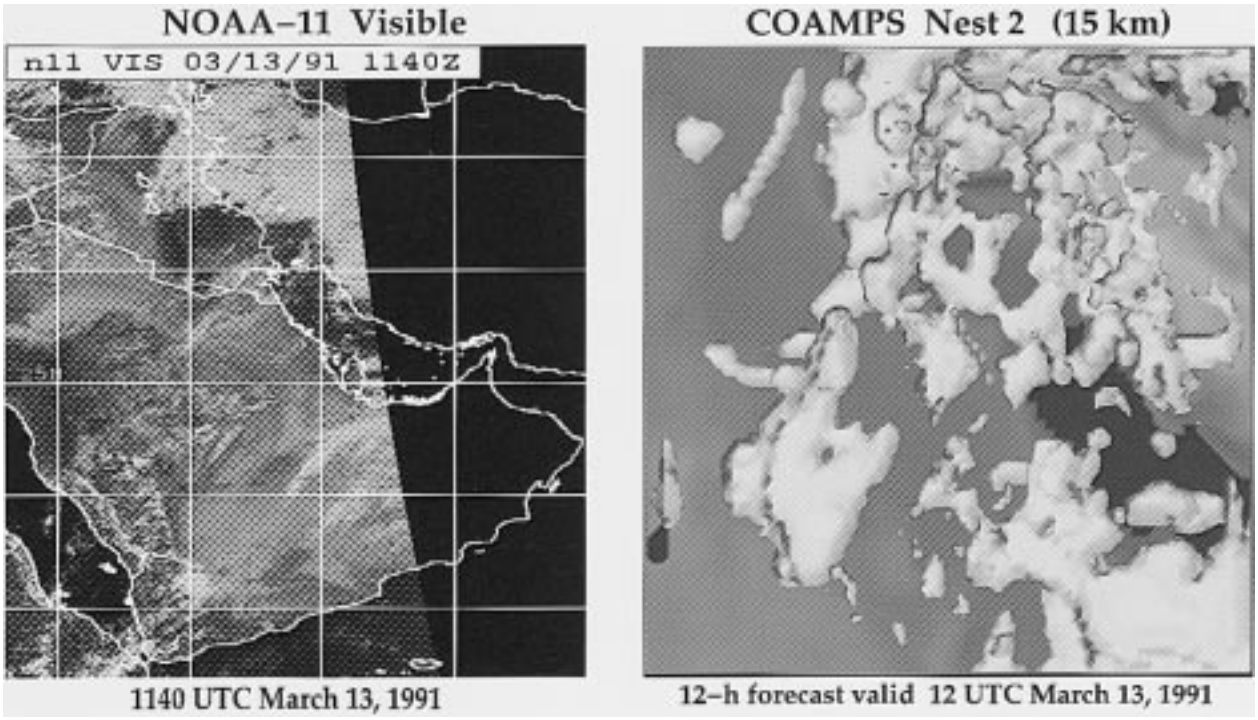

FIG. 11. As in Fig. 8 but (a) for 1140 UTC 13 March and (b) for 1200 UTC 13 March.

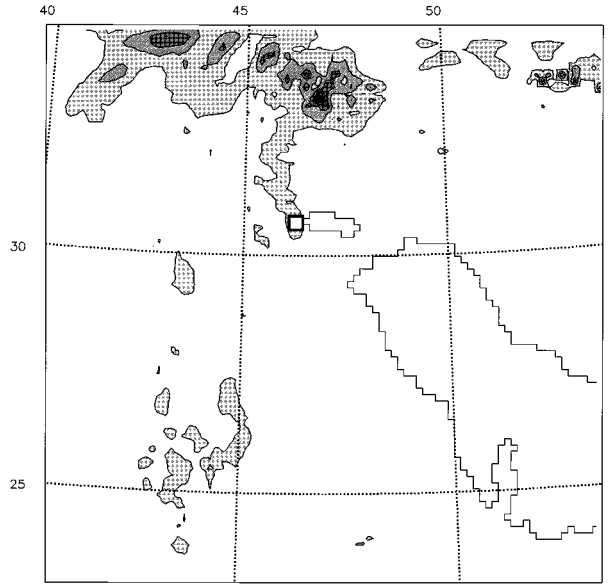

FIG. 12. Simulated accumulated precipitation (units of mm) for 1200 UTC 10 March–1200 UTC 13 March. Contours are drawn every 5 mm from 5 to 65 mm. Maximum value is 63 mm.

Within the Persian Gulf region (20°–40°N, 40°–60°E), the surface pressure time mean difference (1–15 March) of the data denial (DD45) minus the BL reanalysis is slightly negative (−0.1 hPa) and, correspondingly, there is a slightly warmer mean surface air temperature analysis (0.5°C). At the surface the winds in the Persian Gulf region winds have no mean east or west bias, but the winds in the data-denial region have a slightly larger southerly component, corresponding to a positive north–south wind difference (DD45-BL) of 0.2 m s^{-1}. At 500 hPa, the time-mean height error for the entire global reanalysis period is slightly positive (2 m) and the rms height difference is 10 m. The 500-hPa winds demonstrate the same tendency as the surface winds, in that the DD45 assimilation has a tendency to have a slightly larger southerly component than BL. Overall the height anomalies of BL and DD45 are well correlated with each other.

For the specific period of 1200 UTC 10 March–1200 UTC 13 March the principal difference in the BL and the DD45 reanalyses in the Persian Gulf region is for the period 0000 UTC 12 March–0000 UTC 13 March. At 1200 UTC on 10 March the DD45 reanalysis has a slightly deeper surface low (with slightly higher surface winds) centered over central Iran. At 500 hPa the heights are slightly higher (weaker upper trough) in the DD45 experiment than the BL. The trough moving through the region at 0000 UTC 11 March continues to be weaker in the DD45 reanalysis than in the BL. By 1200 UTC the BL and DD45 500-hPa analyses are nearly identical with a shortwave trough over eastern Iran and a small-amplitude ridge over eastern Iraq. At 0000 UTC 12 March, however, the DD45 reanalysis has a marked ridge in the low-latitude westerlies (20°–30°N) over eastern Saudi Arabia, while the BL 500-hPa flow is nearly zonal. By 1200 UTC 12 March, both the BL and DD45 analyses have a marked ridge extending over the Persian Gulf, with a trough entering into the Red Sea region. The DD45 surface winds over southern Iraq are slightly more southerly than the BL surface wind analysis. The BL reanalysis of a surface low centered over western Kuwait for 0000 UTC 13 March has a slightly tighter gradient than in the DD45 reanalysis, although the central pressure was slightly weaker, and the upper trough is slightly deeper in the BL. However, at 1200 UTC 13 March the situation is reversed with the 500-hPa heights lower over the Persian Gulf (and a lower surface pressure) in the DD45 than in BL.

b. Global baseline (BL) analysis versus analysis with random perturbed observations (RPO)

In contrast to the DD45 experiment, the global analysis carried out with a random perturbation of all data types (RPO) demonstrated differences from the BL analysis in all regions of the globe. The time mean for 1–15 March of the Northern Hemisphere's 500-hPa height rms difference in the data analysis is 7.5 m. The corresponding difference of DD45 with the BL is 2.5 m.

In general, over the Persian Gulf region the differences between BL and RPO are smaller than the differences between BL and DD45. Over the Persian Gulf region the rms differences of BL and RPO reanalyses are 25% smaller than comparable rms differences of BL and DD45.

As with the comparison of the DD45 and BL, for the specific period of 1200 UTC 10 March–1200 UTC 13 March the primary difference in the BL and RPO reanalyses in the Persian Gulf region is for 0000 UTC 12 March to 0000 UTC 13 March. At 1200 UTC 10 March both the BL and RPO reanalyses depict a weak surface low centered over central Iran. The 500-hPa heights are slightly higher in the RPO experiment than the BL (the RPO experiment depicted a slightly weaker upper trough). The trough moving through the region on 0000 UTC 11 March is analyzed as slightly weaker in the RPO experiment than the BL but is in better agreement with the BL experiment than the DD45. The weak surface low over Iran is also better depicted in the RPO than the DD45. The BL and RPO experiments' reanalyses are consistent for 1200 UTC 11 March, depicting a weak ridge building over northern Iraq and Iran. Whereas at 0000 UTC 12 March the DD45 reanalysis has a marked ridge in the low-latitude westerlies (20°–30°N) over eastern Saudi Arabia, both the BL and RPO 500-hPa flows are more zonal. By 1200 UTC 12 March, both the BL and RPO reanalyses have a marked ridge extending over the Persian Gulf, with a trough entering into the Red Sea region. Both the BL and RPO reanalyses were very consistent with the magnitude and position of the surface low centered over western Kuwait for both 0000 and 1200 UTC 13 March.

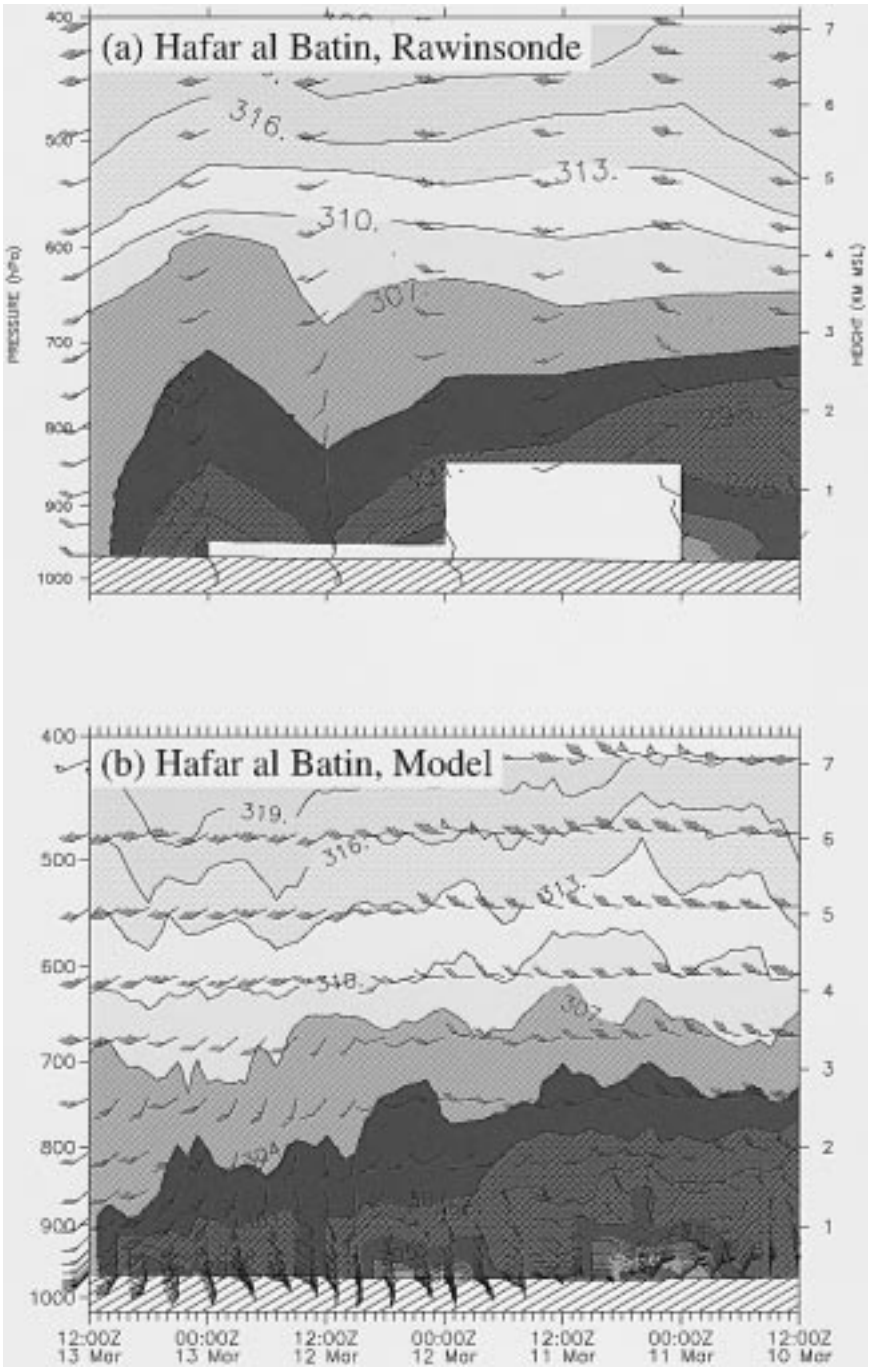

FIG. 13. Time–height cross section of (a) observed and (b) COAMPS forecasts of winds (full barb equals 5 m s^{-1}, or approximately 10 kt) and potential temperature (color, contour interval of 3 K) at Hafar Al Batin (see Fig. 1) from 1200 UTC 10 March to 1200 UTC 13 March. COAMPS forecasts are shown for every hour while observations are every 12 h. White blocked regions indicate missing data.

c. Comparison of COAMPS reanalyses

The alternative analyses of NOGAPS suggests that there was no significant variability caused by analysis or observation errors at the synoptic scale. Now the mesoscale variabilities of alternate COAMPS analyses will be examined. The 15-km analyses will be used for geopotential height because the 5-km grid is small and

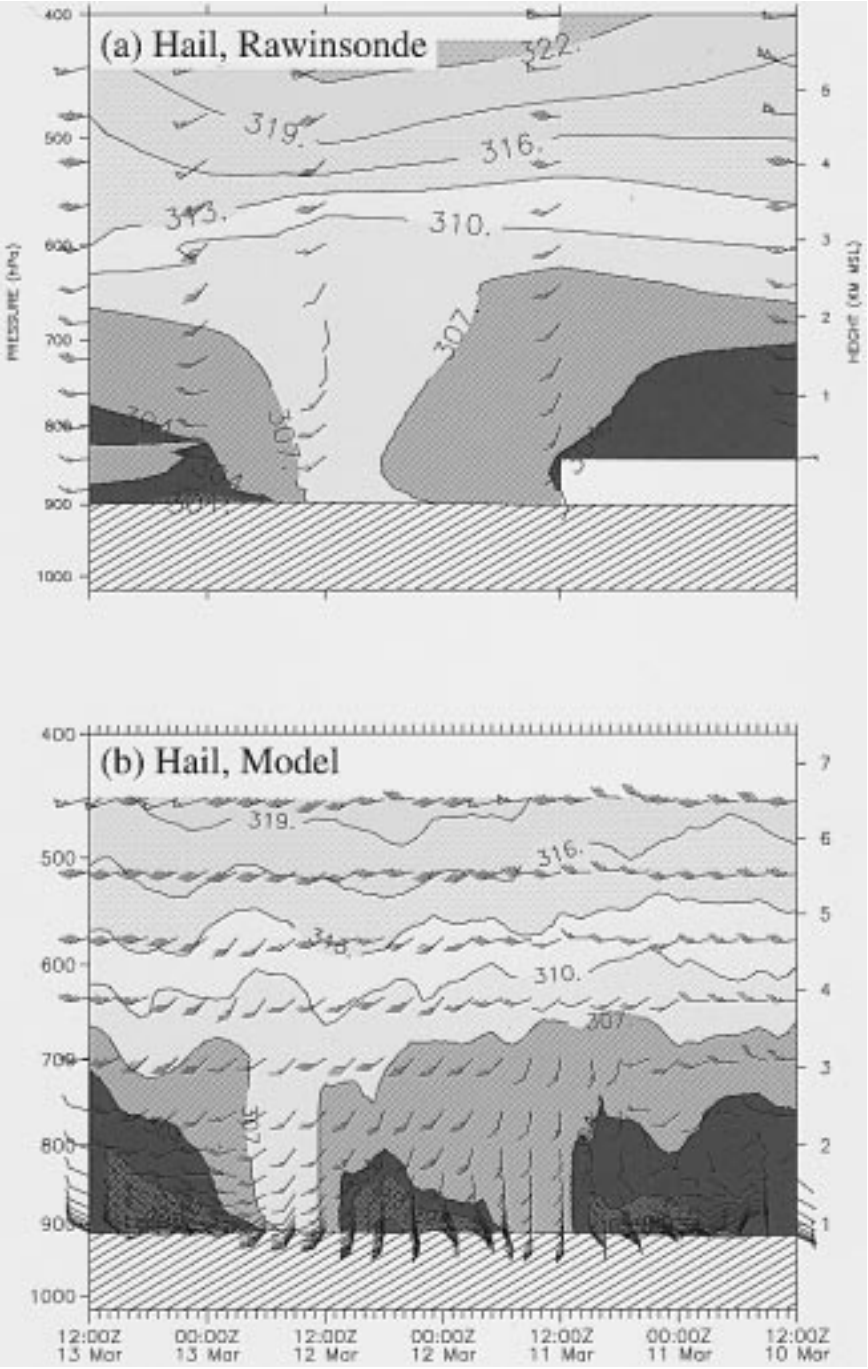

FIG. 14. As in Fig. 13 but for Hail (see Fig. 1).

has few observations for comparison. For model winds, we use side-by-side comparisons of the observations and the reanalyses.

The sensitivity to the observations of COAMPS can be illustrated by the bias and rms errors in geopotential heights at standard pressure levels over the 15-km domain during the period from 1200 UTC 10 March through 1200 UTC 13 March. As depicted in Fig. 18, the geopotential errors in general are small in the midtroposphere and larger at the surface and at the tropopause level, a characteristic consistent with typical performance of weather prediction models. Specifically the height biases of the COAMPS baseline analysis BL decreases from -5 m at the 1000-hPa level to ± 2 m above 850 hPa. The biases increase above the 300-hPa level, reaching a maximum of 12 m at 200 hPa. The rms errors

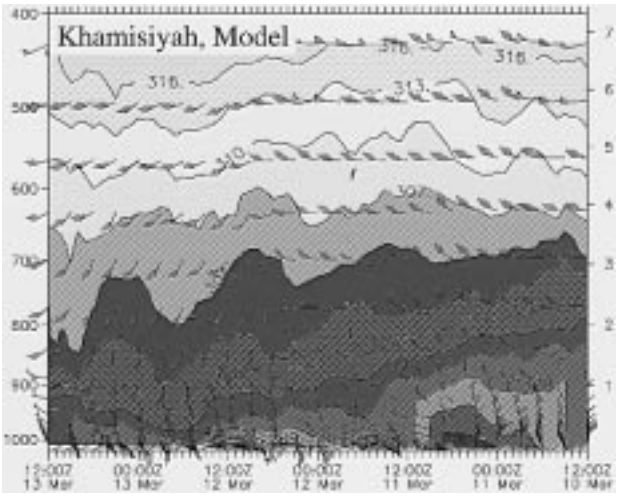

FIG. 15. As in Fig. 13 but for Khamisiyah. Only the simulation is shown since no rawinsonde was available.

in geopotential height of BL are 15 m at the 1000-hPa level and 10 m at 925 hPa, increasing to 30 m at the 200-hPa level. These errors are smaller than typical 12-h forecast errors. For example, in a 2-week COAMPS validation test performed over the same region, the height bias and rms error were −8 and 25 m at 1000 hPa, −2 and 24 m at 500 hPa, and 1 and 60 m at 200 hPa. Junker et al. (1989) presented errors of similar

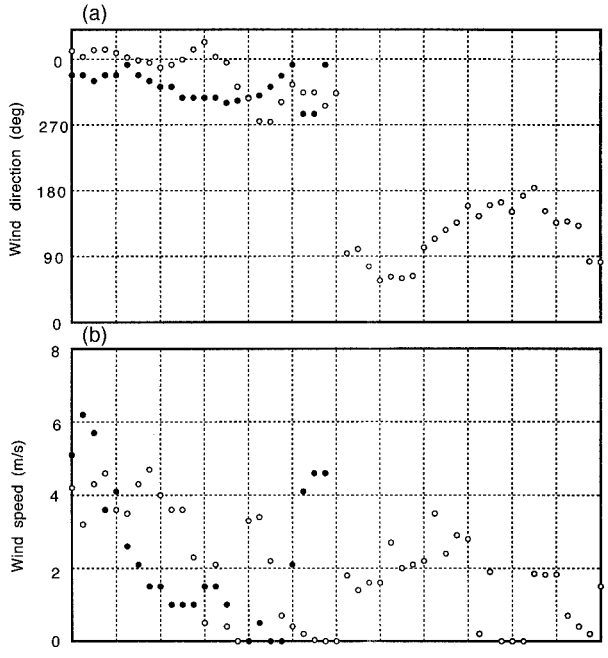

FIG. 16. Observed 2-m wind direction and speed (m s^{-1}) at mobile USAF station (AF1 in Fig. 1; solid circles) along with 12-h COAMPS forecasts (open circles) and 12-h COAMPS analyses (asterisks) for 0000 UTC 9 March–1200 UTC 12 March) at 10 m. USAF data were unavailable after 1200 UTC 11 March.

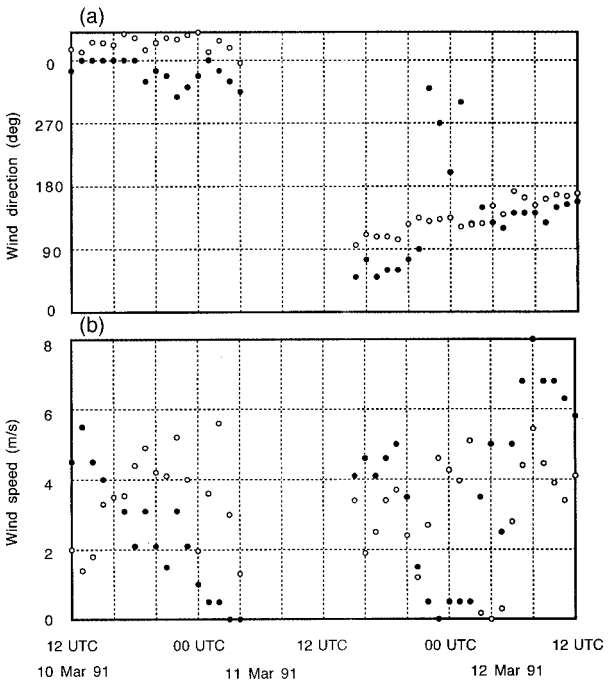

FIG. 17. As in Fig. 16 but for USAF station AF2 (Fig. 1) for the first 24 h and AF3 for the last 30 h.

magnitude for the Limited Fine Mesh Model and the Nested Grid Model.

All the alternative analyses have larger errors as compared to the BL analysis. For example, the geopotential height biases of the alternative analyses range from −13 to −8 m at 1000 hPa and from 18 to 32 m at 200 hPa. The rms errors are 34–46 m at the 200-hPa level. Overall, DD45 has the highest bias and rms errors. As stated before, the COAMPS DD45 reanalysis is equivalent to a forecast with analyzed boundary conditions but without any data assimilation. The behavior of the alternative analyses is not surprising. One would expect degraded analyses when observations are denied over a large portion of the model domain or random errors are added to the observations.

TABLE 1. Description of alternative reanalyses used in this study.

Reanalysis	Abbreviated name	Characteristics
Baseline	BL	Standard data assimilation cycle
Data denial on 15-km grid	DD15	Data denied to COAMPS inside 15-km grid
Data denial on 45-km grid	DD45	Data denied to COAMPS and NOGAPS inside COAMPS 45-km grid
Perturbation of observations	RPO	All global observations randomly perturbed prior to QC and data assimilation for NOGAPS and COAMPS

TABLE 2. Observation-error standard deviations (from Goerss and Phoebus 1992).

Press. (hPa)	Height (m) Raob	u or v wind (m s^{-1}) Raob/Pibal	Aircraft	Cloud track
1000	6.0	2.2	3.0	2.8
925	6.0	2.2	3.0	2.8
850	6.0	2.2	3.0	2.8
700	6.0	2.2	3.0	3.8
500	9.0	2.8	3.0	4.8
400	10.0	3.0	3.5	5.8
300	12.0	3.2	4.0	6.5
250	13.0	3.1	4.0	6.5
200	14.0	3.0	4.0	6.5
150	15.0	2.8	4.0	6.5
100	16.0	2.8	4.0	6.5
70	17.0	2.8	4.0	6.5
50	19.0	2.8		
30	24.0	2.8		
20	29.0	2.8		
10	40.0	2.8		

Surface u or v wind (m s^{-1}) F Buoy	Island Buoy	CMAN	Ship SSM/I
1.8	1.9	2.2	2.4

Surface height (m) F Buoy	PAOB	Other
4.0	20.0	7.0

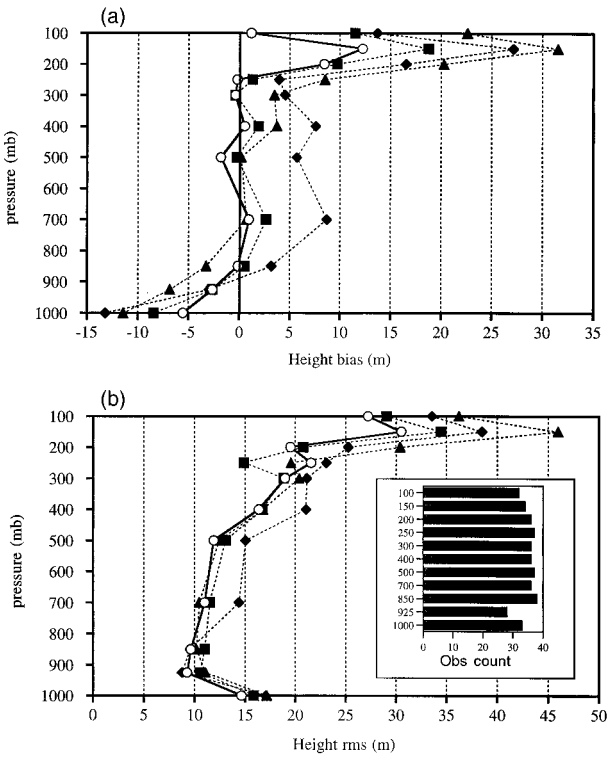

FIG. 18. Rms and bias for COAMPS reanalyses of geopotential heights (m) over the 15-km domain for the period 1200 UTC 10 March–1200 UTC 13 March. The reanalyses are defined as follows: open circles, BL; closed triangles, RPO; closed squares, DD15; and closed diamonds, DD45. Five to seven rawinsonde profiles were available at each synoptic time. The total number of observations at each pressure level is shown in the inset.

We have shown statistical comparisons of the alternative analyses with rawinsonde stations above. The accuracy of the reanalyses locally is also important since these winds and boundary layer structures are directly applied in dispersion models to calculate the dosage. For comparison, meteograms of observations and reanalyses at Hafar al Batin and Hail were plotted (Figs. 19 and 20). At Hafar al Batin, all the analyzed wind speeds are within 2.5 m s^{-1} of the observation. Consistent with the sounding, all four analyses show an anticyclonic turning of the wind from NNW to SSW and then to WSW during the 72-h period after the release. The observed diurnal temperature variation and the warming accompanying the onset of the southerly wind component are depicted in the four analyses. At these two stations, the surface temperatures at 0000 and 1200 UTC in the COAMPS BL analysis are within 1°C of the observed. DD45 has the coolest temperature and highest wind speeds. In agreement with the statistical comparison, the BL appears to be the most consistent analysis overall as compared to the observation. At Hail, the onset of the southerly component was 12 h earlier, around 1200 UTC March 11. The observed general near-surface meteorological conditions are reproduced in the analyses. Again the BL is the best overall analysis whereas DD45 has the largest temperature and wind speed differences.

As suggested in a field experiment emulating the demolition at Khamisiyah conducted at Dugway Proving Ground, a large portion of the nerve gas released at Khamisiyah most likely leaked onto the surface soil and the wooden crate from the Iraqi chemical weapons and then evaporated over several days. Hence, the local winds at Khamisiyah are important for several days for the calculation of downwind transport of chemical agents. The meteogram shown in Fig. 21 illustrates the differences among the four analyses at Khamisiyah. Disregarding the very light wind situations, all the wind directions lie within a 30° angle of each other. The general trend of wind direction turning from NNW to SSW around 0000 UTC March 12 is captured in all four analyses. The 10-m temperatures all feature a diurnal variation and a general warming after the onset of the southwesterlies. The DD45 analysis again has the coolest surface temperature.

These comparisons suggest that quantitatively different analyses can be produced when data were denied or random errors were introduced. However, the general atmospheric characteristics were not altered to any large extent even on the mesoscale. The effect of the seemingly small differences among the alternative analyses on the transport of the released agents will be demonstrated next.

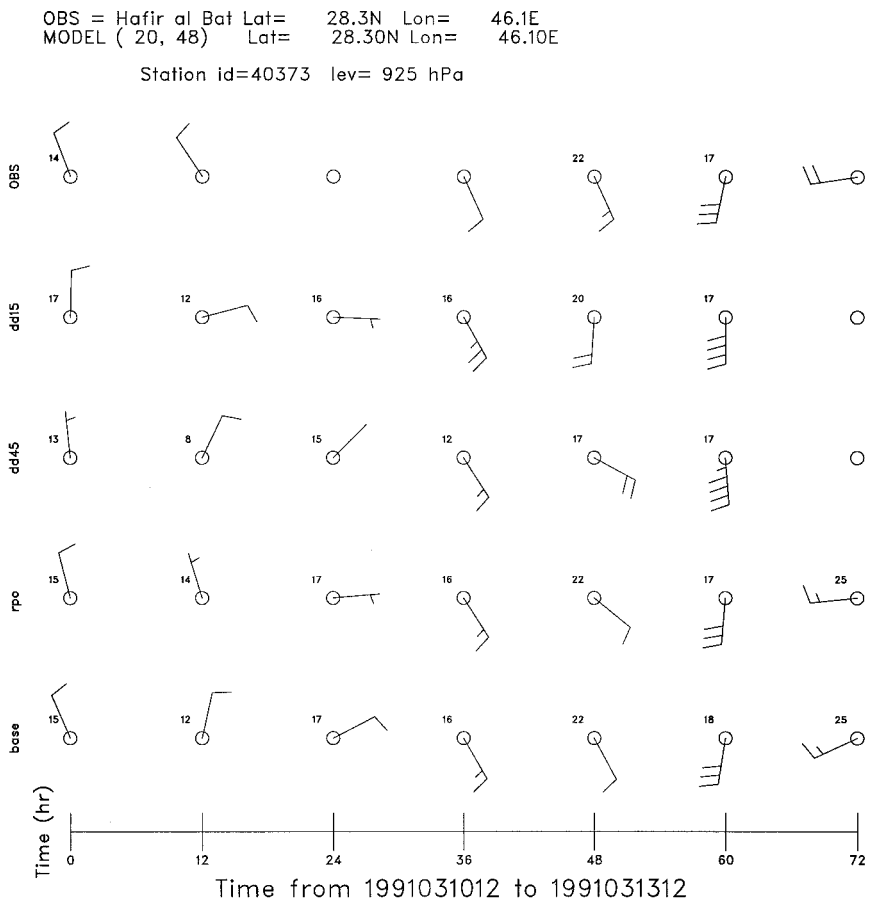

FIG. 19. Meteogram of 925-mb winds at Hafar Al Batin for the period 1200 UTC 10 March–1200 UTC 13 March. Rawinsonde observations are given in the top row. The baseline and alternate reanalyses are given in the subsequent rows. A full barb = 5 m s^{-1}, or approximately 10 kt.

5. Transport simulations

The above sections have described the meteorology of the Kuwait region during the time of the destruction of the Khamisiyah munitions depot as well as the sensitivity of the models to the lack of observations or to perturbed observations. The quantity of interest to those studying the epidemiology of Gulf War Illnesses is the dosage, defined as the integral of the concentration over time. In the absence of an observational network, the dosage can only be estimated with T&D models driven with the predicted time-dependent wind fields and thus incorporating the effects of diurnal variations in the boundary layer, the approaching surface low, and the frontal passage. T&D models suitable for quantitative estimates are described in Sherman (1978), Sykes et al. (1984), and Draxler et al. (1994). As mentioned before, the NOGAPS and COAMPS reanalyzed fields were given to other agencies and used to drive some of these T&D models.

However, the goal of the transport calculations reported here is to obtain a first-order estimate of the sensitivity of the gross features of the dosage patterns to the different dynamical forcings. For this, the chemistry and microphysics peculiar to the nerve agents can be neglected. The 5-km COAMPS fields are useful for transport for short periods near the source. However, due to the long estimated duration of the release (36 h), and the possible sensitivity to low concentrations, extended simulations (72 h) were required during which much of the gas leaves the 5-km domain. Therefore, the results shown here are from the 15-km calculations. This study utilizes a simplified version of the Eulerian aerosol and chemistry model of Toon et al. (1988) driven by the dynamic and thermodynamic fields from the 15-km resolution COAMPS fields at 1-h intervals. Although the transport calculations were carried out to 72 h, the COAMPS fields that were used came from a series of 12-h forecasts, each followed an analysis to create the first guess for the next data assimilation cycle. The COAMPS vertical diffusion coefficients are used in the transport calculation, but a smaller constant horizontal diffusion coefficient of 5×10^3 m^2 s^{-1} is applied. It is assumed that there is no deposition of the gas for a worst-case scenario. The finite element method used to

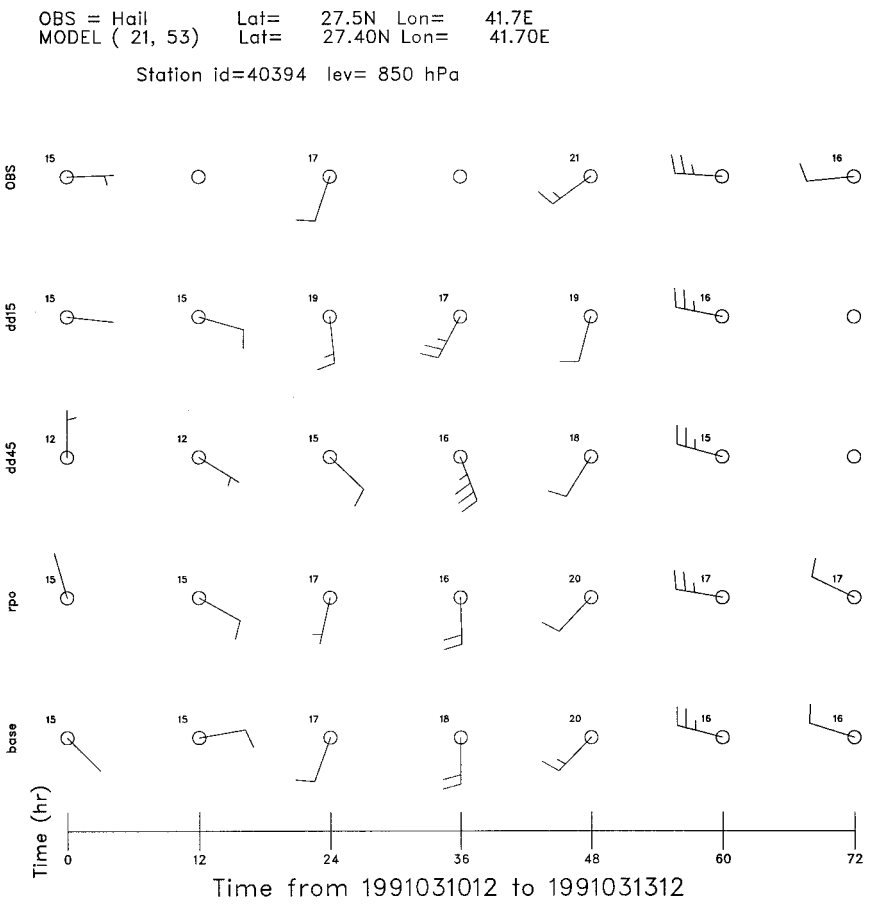

FIG. 20. As in Fig. 19 but for Hail and at 850 mb.

solve the advection–diffusion equation has the desirable characteristic of conserving mass and usually preserves peak concentrations, but it is diffusive, as are most numerical schemes, when the source is a single grid point, as is the case in these simulations. This method is expected to overestimate the spatial coverage of the agent and underestimate the peak concentrations, yet should yield reasonable dosage patterns along the axis of the dosage plumes, meeting the needs of this study.

The transport calculations require a characterization of the source term, including the location, time, strength, and duration of the emission. The location is well known, as is the time of the detonation. The event took place at 30°44′32″N, 46°25′52″E (Fig. 1) at 1315 UTC 10 March. In contrast, the strength and duration are poorly known due to uncertainties in the number of rockets and the incomplete destruction of the rockets. The most likely source is from 320 rockets each with 6.3 kg of nerve agent of 50% purity, for a total of 1008 kg. The maximum source is from 650 rockets for a total of 2048 kg, and the minimum source is from 170 rockets with 536 kg.

First-hand reports from Khamisiyah and from tests conducted in June 1997 at Dugway point toward the likelihood of as little as 5% immediate vaporization and combustion of the agent with the remainder slowly evaporating from the damaged rockets, the wood containers, and the sand. Even with the best-designed field experiments, the rate of evaporation of agents at Khamisiyah is difficult to determine, but probably occurred over a period of 12 h to several days.

To avoid the uncertainty concerning the fashion in which the chemical agents are released, and to simplify the discussion, two different simple emissions were assumed for the transport calculation: a uniform evaporative emission of 1000 kg over 36 h and an instantaneous emission of 1000 kg, both beginning at 1330 UTC. The former emission duration is more similar to the recent estimates from the Dugway experiment. In both cases, all of the agent is released into the lowest model layer. Since the emphasis of the transport calculations is to understand the transport patterns and the sensitivity to the meteorology, the absolute amount of agent released is not important. Accordingly, only the patterns of the normalized concentration and dosage are emphasized in the following discussion, rather than the absolute amounts.

In addition to sensitivity tests utilizing the four me-

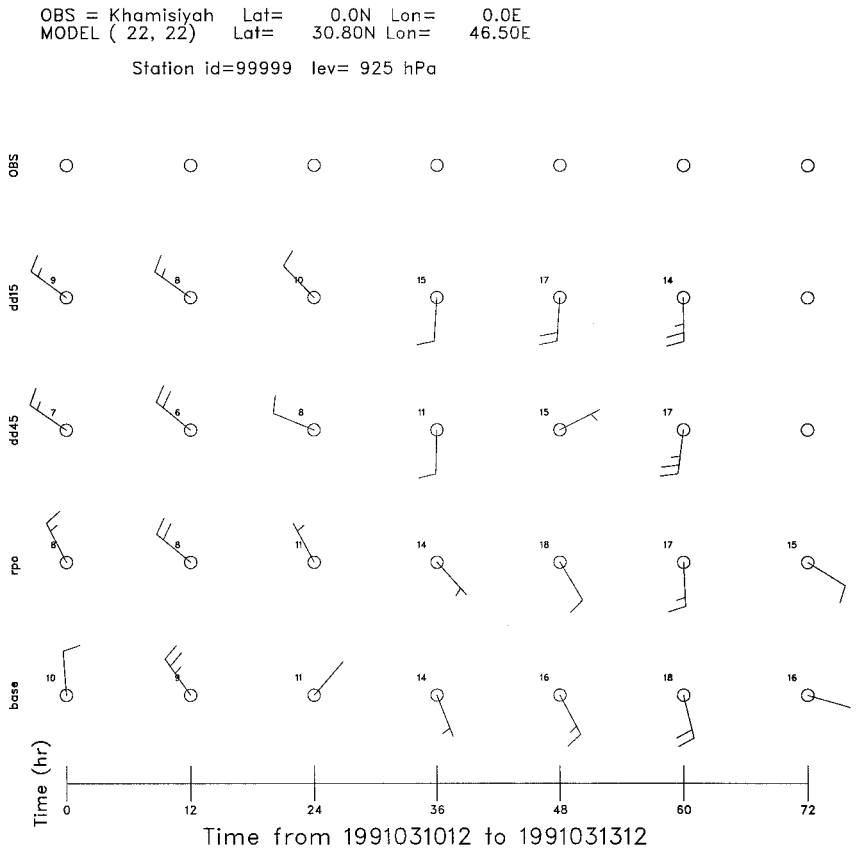

FIG. 21. As in Fig. 19 but for Khamisiyah and at 10-m height. No observations were made at Khamisiyah.

teorological datasets and the two emission scenarios, the source is perturbed in space and time. For the location perturbations, the source is moved 120 km in the north, south, east and west directions. For the time perturbations, the emission is moved ahead and back in time by 1 h. Of course there is no uncertainty in the time or location of the demolition. These six perturbations are utilized to illustrate the effects of error in the timing and location of meteorological features described in section 3. When presenting and comparing these results, the final dosage patterns from the location-perturbation simulations are translated back to Khamisiyah. The two time-perturbation simulations are not translated since these used Khamisiyah as the location of the source.

To summarize, there are four meteorological datasets (Table 1), two emission scenarios, and seven source variations for a total of 56 transport calculations (Table 3). Of these, the ''baseline'' calculation is defined as that using the baseline COAMPS simulation (BL), the 36-h evaporative release of 1000 kg, and a source at Khamisiyah at 1330 UTC. In the discussion that follows, we first present the baseline dosage and concentration distribution. Then a comparison with the other 55 simulations is made, primarily through an intercomparison of the dosage distributions.

TABLE 3. Characteristics of baseline and sensitivity transport simulations.

Parameter	Baseline value	Perturbation values
Reanalysis dataset (See Table 1)	BL	DD15, DD45, RPO
Emission duration	36 h	Instantaneous
Location	Khamisiyah	±120 km N, S, E, and W of Khamisiyah
Time of emission	1330 UTC 10 March 1991	1230 or 1430 UTC

a. Baseline simulation

The baseline dosage pattern (Fig. 22a) shows two predominant features. There is a curving branch to the southwest resulting from persistent anticyclonic conditions during the first 12 h of emission (Figs. 7a and 7b). The winds are light and westerly over the next 12 h and the gas remains in the area. After 1200 UTC 11 March, the wind shifts rapidly to southeasterly and remains from that direction until the surface low arrives at Khamisiyah at 1000 UTC 13 March. Thus, the final

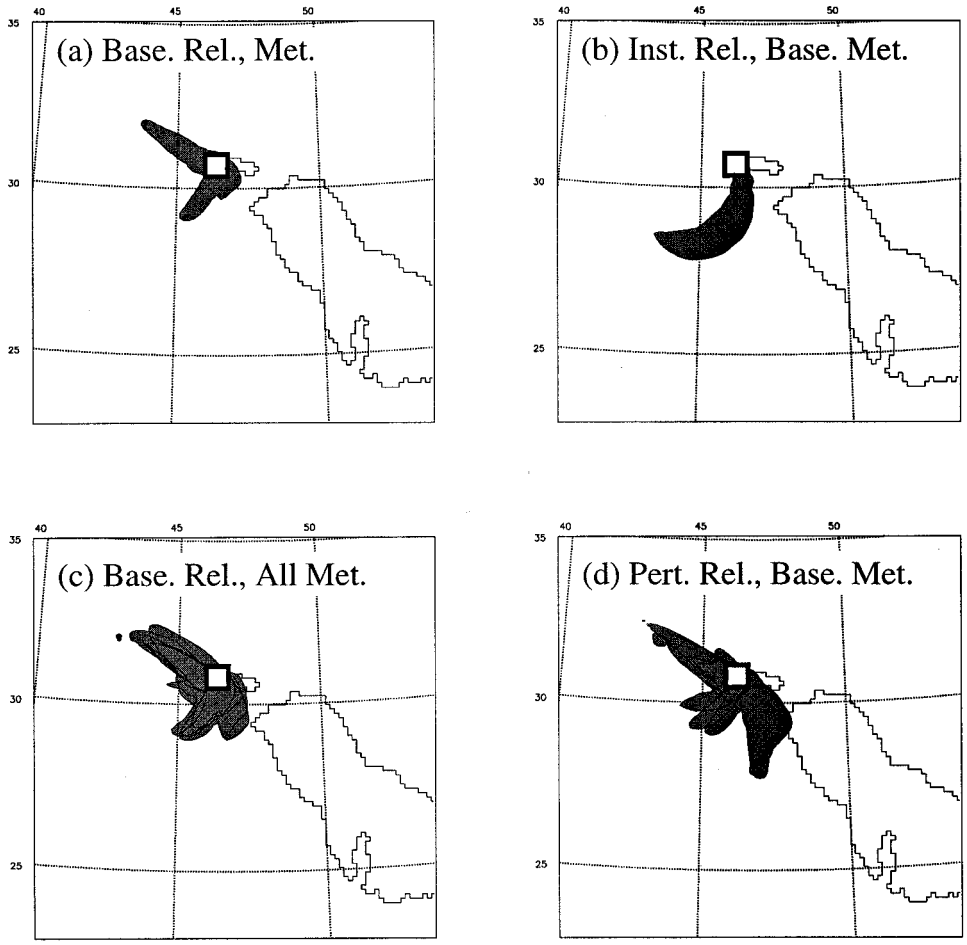

FIG. 22. Simulated dosage patterns for 1200 UTC 10 March–1200 UTC 13 March: (a) baseline emission and baseline reanalysis, (b) instantaneous release and baseline reanalysis, (c) baseline release and all four reanalyses, and (d) location- and time-perturbation releases and baseline reanalysis.

12 h of the 36-h emission are in southeasterly winds leading to the NW branch of the dosage pattern. After the low passes Khamisiyah, some of the gas is brought back into the region in the NW flow behind the low, though these concentrations are too low to contribute noticeably to the dosage pattern.

The vertical distribution of the agent is controlled by boundary layer mixing. The simulated emission began at 1330 UTC, or 1630 local time, in the late afternoon. The gas released in the first few hours was immediately mixed throughout the kilometer depth of the boundary layer (Fig. 23a). After sunset, the boundary layer stabilized and subsequent emissions were concentrated in the lowest few hundred meters capped by the inversion. For example, at 0000 UTC, or 0300 local time, the concentrations were four times higher at the surface (Fig. 23b) than at 1400 UTC. After sunrise the next day, the gas was again mixed throughout the boundary layer and surface concentrations decreased. The gas was again trapped in the lower boundary layer after sunset on 11 March in the southeasterly flow (not shown).

Figure 23 and the time sections of rawinsonde and model data (Figs. 13–15) reveal persistent westerlies above the PBL for much of the period. Small amounts of agent reach these heights and are advected eastward over the Persian Gulf (not shown). Wet removal of the agent was ignored in the simulations. The small amounts of modeled accumulated rainfall for the 3-day period (Fig. 12) supports this assumption.

b. Sensitivity studies

In the instantaneous emission simulation, all of the gas is emitted in the NNW wind pattern that dominated Khamisiyah after the detonation. The resultant dosage pattern (Fig. 22b) is similar to, though more extensive than, the southwest branch in the baseline simulation (Fig. 22a). With the instantaneous emission, none of the agent is emitted in the presence of the nocturnal inversion and the fumigation process is averted (Fig. 24). Even so, the concentrations and dosages are higher since all 1000 kg are emitted instantaneously. The northwest

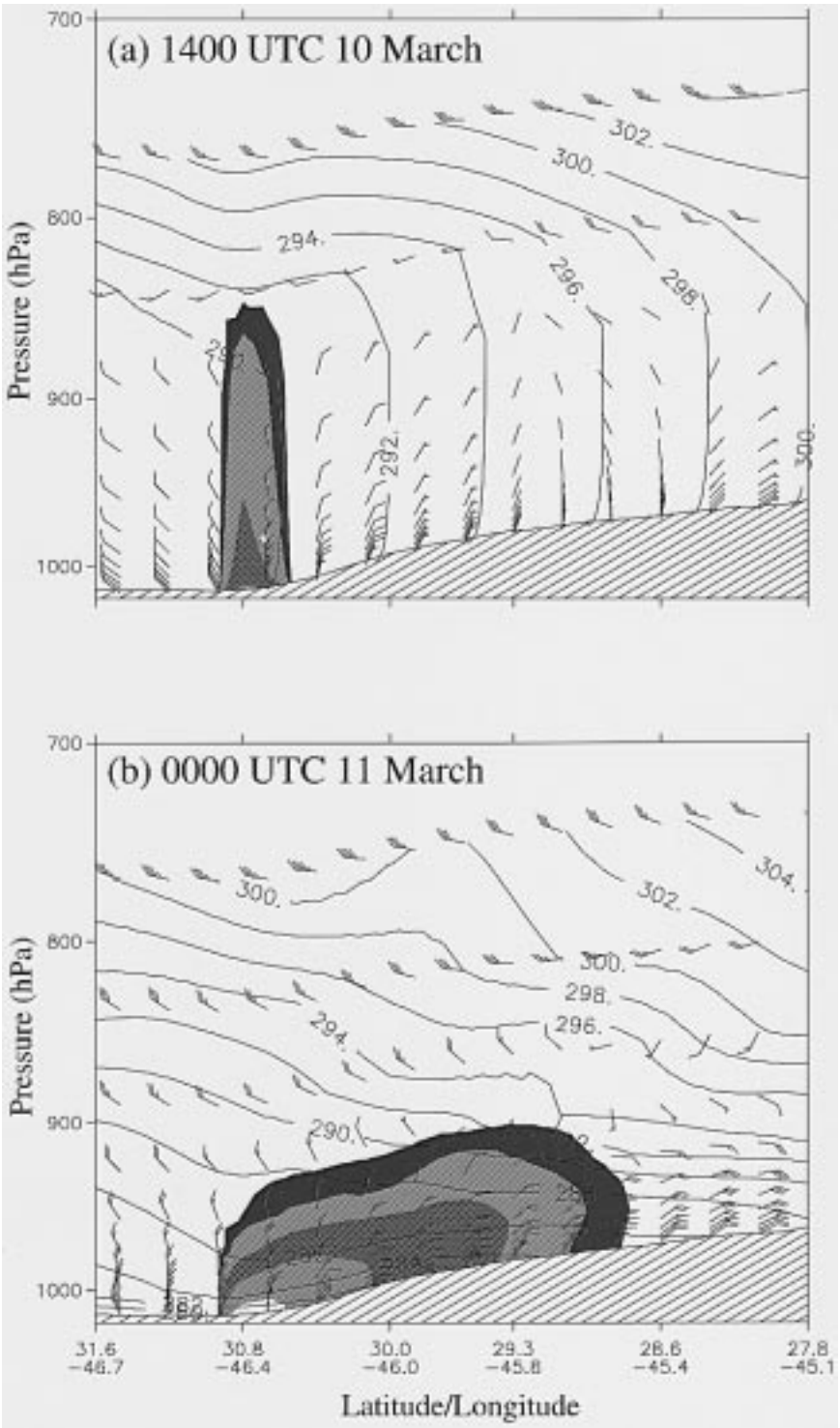

FIG. 23. Cross section from 31.6°N, 46.7°E to 27.8°N, 45.1°E (NNE–SSW through Khamisiyah) of simulated gas concentration (arbitrary units, with two shaded contours per decade) for the baseline emission and baseline reanalysis. Also shown are potential temperature (contoured every 2 K) and wind speed and direction (wind barbs, with a full barb equal to 5 m s^{-1}): (a) 1400 UTC 10 March and (b) 0000 UTC 11 March.

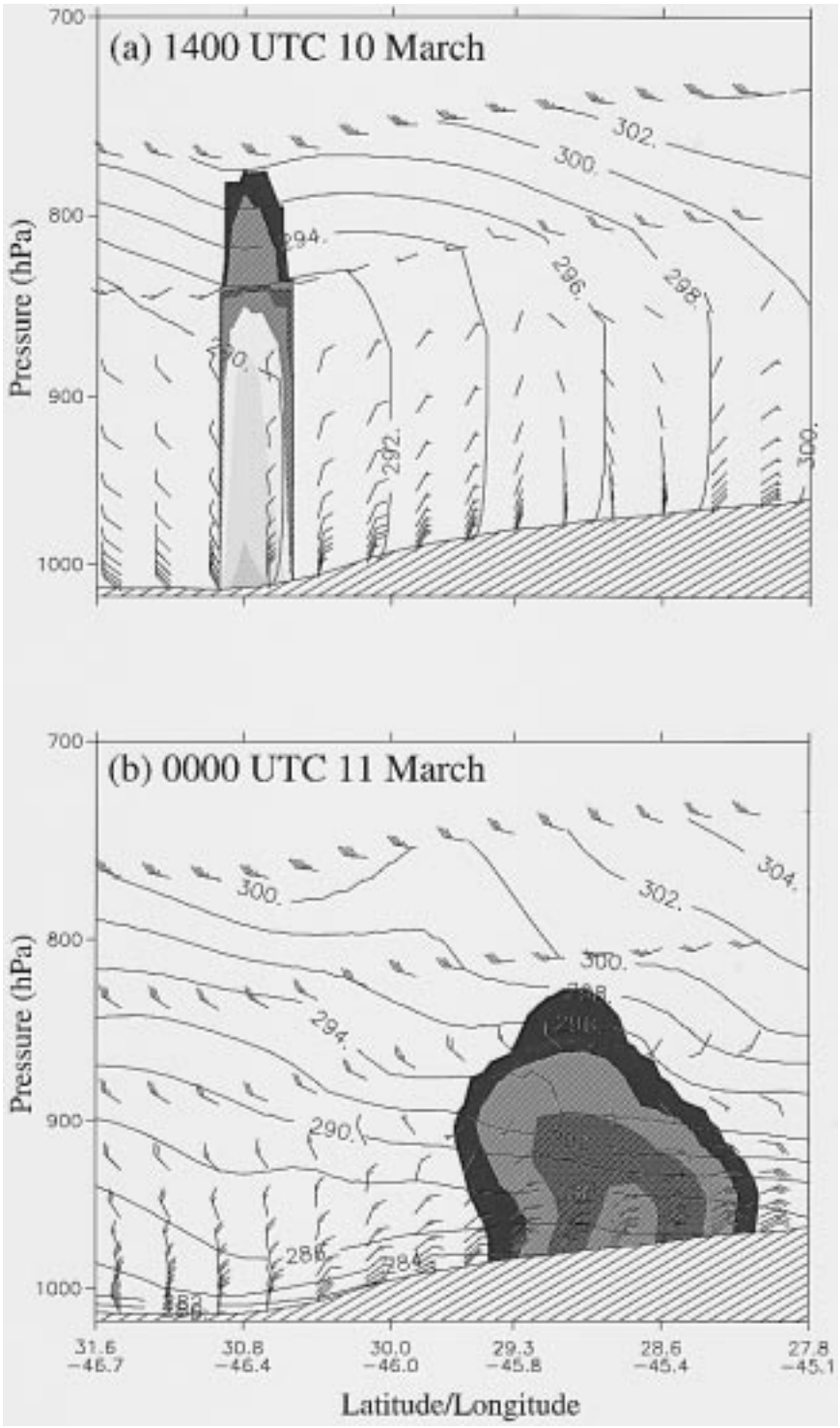

FIG. 24. As in Fig. 23 but for the instantaneous release.

branch is absent since none of the agent was emitted during the time of the southeasterly flow at Khamisiyah.

The significance of differences in the reanalyses is illustrated by comparing the dosages for the simulations that use the 36-h baseline emission and the four reanalyses datasets. All of the dosage patterns (Fig. 22c) contain the southwesterly and the northwesterly branches. A third branch to the SSE appears in the DD45 and RPO simulations. This branch is formed by transport in NNW winds during the first few hours of the simulations

(Fig. 7a). This feature is nearly absent in the BL and DD15 simulations. The differences between the direction and extent of the southwest and northwest branches are small.

The sensitivity to the location and timing of meteorological features is illustrated by comparing the dosage patterns for the baseline simulation with those where the time and location of the release were perturbed (Table 3). These results are shown in Fig. 22d. These patterns exhibit the same three arms as in other baseline emission (36-h release) shown in Figs. 22a and 22c. However, the variability is large compared to the cases where the different reanalyses were used (Fig. 22c), in particular the southern branch for the east and north source displacements. The analyses of surface winds (Figs. 7a and 7b) show that the surface winds to the north and east of Khamisiyah are stronger causing longer transport.

6. Summary and conclusions

Global and mesoscale reanalyses have been conducted to obtain the atmospheric conditions in early March 1991 over southern Iraq in support of the study of the release of chemical agents from the destruction of an Iraqi ammunition depot at Khamisiyah. The global reanalysis was conducted with NOGAPS at a spatial resolution of approximately 80 km and 18 vertical layers for 18 February–15 March 1991. The mesoscale reanalysis, using the global reanalyzed fields as boundary conditions, was conducted with the triply nested COAMPS at spatial resolutions of 45, 15, and 5 km and 30 vertical layers.

As seen from the global reanalysis, the large-scale circulation featured a split of the westerlies over western Europe with the northern branch curving over the Baltic Sea and the southern branch covering the Mediterranean and the Middle East. The synoptic conditions in this post-Shamal, transitional period was controlled by eastward-propagating small-amplitude troughs and ridges. On the mesoscale, the condition over the lower Tigris–Euphrates Valley was further modulated by the diurnal variation in the local circulations between land, the Persian Gulf, and the Zagros Mountains. The boundary layer winds at Khamisiyah were northerly or northwesterly at the time of the detonation, shifting to the west-northwest in the nocturnal boundary layer. On the second day, the wind direction quickly shifted to easterly and then southeasterly as a high passed north of Khamisiyah and a new low pressure center built over the Red Sea. On the third and final day, the region was dominated by the approach and passage of the low pressure system and the associated front with cyclonically veering winds that eventually changed to northwesterlies by 0000 UTC 14 March. Despite the presence of the low, the precipitation amounts in the study area were negligible and unlikely to have had an effect on the nerve agent.

Data-denial and perturbation analyses were also conducted to assess the uncertainties in the above baseline reanalysis due to observation and analysis errors. In the two data-denial experiments, observations in the COAMPS 15-km and the 45-km grid domains were denied. For the perturbation reanalyses, random standard observation errors were added to all observations used in the reanalysis. In each of the alternative analyses, the differences with respect to the baseline reanalysis were within the typical error bounds of meteorological analysis. This suggests the reanalysis had bounded variability and the atmospheric conditions were unlikely to differ from the reanalysis significantly.

For the range of meteorological conditions applied for our transport calculations, the agent from the 36-h evaporative release most likely was transported somewhere through the azimulthal section between 160° and 315° (S through NW). The dosages from the different reanalyses simulations are more consistent than are the simulations where the source location is perturbed in space or time. Given the inherent uncertainty in numerical weather analysis and prediction, the uncertainty in the source term, and the sensitivity of the modeled dosage patterns to the four different meteorological datasets, it is impossible to pinpoint the location of a narrow plume nerve agent that might have contaminated the U.S. and U.N. troops near Khamisiyah. It is only prudent that we approach the final determination of the plume location, at least as far as atmospheric conditions are concerned, from an ensemble consideration. For that, this study has presented some possibilities.

This study demonstrates the value of the reanalysis procedure for problems of interest to the navy and the other armed services. A mesoscale prediction and data assimilation system embedded and driven by a global system is a powerful method for obtaining meteorological conditions and is essential for studies of continuous or instantaneous emissions of chemical or biological agents, or other naturally occurring aerosols such as smoke and dust. The analyzed fields over the mesoscale domain can be used for near-field transport and dispersion, and the global fields can be used for long-range transport. The current global and mesoscale prediction systems at NRL are also proven to be capable of supporting dispersion models in future chemical and biological (CB) defense warfare, antiterrorist urban warfare, or in the disposition of CB weapons in compliance with counterproliferation treaties. An even more complete system with a dispersion model embedded within COAMPS is now being developed at NRL. Recent development of an adjoint-based technique to determine the sensitivity of initial conditions, as demonstrated in Fronts and Atlantic Storm-Track Experiment (FASTEX) and North Pacific Experiment (NORPEX-98) (GLR; Langland et al. 1999, manuscript submitted to *Bull. Amer. Meteor. Soc.*) will be invaluable in assessing the uncertainties in postanalysis and in real-time predictions. The adjoint of COAMPS is currently being de-

veloped. When available, these will allow us to make quantitative estimates of the initial condition sensitivity of dynamical forecasts and the dosage predictions.

Acknowledgments. This study has benefited from discussions on meteorological analysis with members of the panel formed by the Institute for Defense Analysis to study the Khamisiyah event, especially Drs. Kerry Emanuel and Richard Reed. We have also benefited from discussions with Central Intelligence Agency analysts. The effort was jointly supported by U.S. Navy SPAWAR, OATSD (NCB), and OSAGWI under Program Element 0902198D. Computational resources were generously provided by FNMOC, Monterey, California. Some of the archived data were provided by FNMOD at Asheville. Satellite images were obtained from the NCAR KuDA database. The NOAA–NASA AVHRR Oceans Pathfinder SST data were obtained from Ms. Vickie Halliwell at RSMAS, University of Miami. We would also like to thank Soheila Judy for formatting and editing this manuscript.

REFERENCES

Arakawa, A., and W. H. Schubert, 1974: Interaction of a cumulus cloud ensemble with the large-scale environment, Part I. *J. Atmos. Sci.,* **31,** 674–701.

Baker, N. L., 1992: Quality control for the navy operational atmospheric database. *Wea. Forecasting,* **7,** 250–261.

——, 1994: Quality control of meteorological observations at Fleet Numerical Meteorology and Oceanography Center. Naval Research Laboratory Rep. NRL/FR/7531-94-9451, 23 pp. [Available from Naval Research Laboratory, 7 Grace Hopper Ave., Monterey, CA 93943-5502.]

Barker, E. H., 1992: Design of the navy's multivariate optimum interpolation analysis system. *Wea. Forecasting,* **7,** 220–231.

Davies, H. C., 1976: A lateral boundary formulation for multi-level prediction models. *Quart. J. Roy. Meteor. Soc.,* **102,** 405–418.

Draxler, R. R., J. T. McQueen, and B. J. B. Stunder, 1994: An evaluation of air pollutant exposures due to the 1991 Kuwait oil fires using a Lagrangian model. *Atmos. Environ.,* **28,** 2197–2210.

Errico, R., and D. Baumhefner, 1987: Predictability experiments using a high-resolution, limited area model. *Mon. Wea. Rev.,* **115,** 488–504.

Gelaro, R., R. Buizza, T. N. Palmer, and E. Klinker, 1998: Sensitivity analysis of forecast errors and the construction of optimal perturbations using singular vectors. *J. Atmos. Sci.,* **55,** 1012–1037.

Gibson, R., P. Kallberg, and S. Uppala, 1996: The ECMWF re-analysis (ERA) project. *ECMWF Newsletter,* **73,** 7–17. [Available from Director, ECMWF, Shinfield Park, Reading RG2 9AX, United Kingdom.]

Goerss, J. S., and P. A. Phoebus, 1992: The navy's operational atmospheric analysis. *Wea. Forecasting,* **7,** 232–249.

Haltiner, G. J., and R. T. Williams, 1980: *Numerical Prediction and Dynamical Meteorology.* Wiley and Sons, 477 pp.

Harshvardhan, D. Randall, and T. Corsetti, 1987: A fast radiation parameterization for atmospheric circulation models. *J. Geophys. Res.,* **92,** 1009–1016.

Hodur, R. M., 1997: The Naval Research Laboratory's Coupled Ocean/Atmosphere Mesoscale Prediction System (COAMPS). *Mon. Wea. Rev.,* **125,** 1414–1430.

Hogan, T., and T. Rosmond, 1991: The description of the Navy Operational Global Atmospheric Prediction System's spectral forecast model. *Mon. Wea. Rev.,* **119,** 1786–1815.

——, and L. R. Brody, 1993: Sensitivity studies of the navy's global forecast model parameterizations and evaluation of improvements to NOGAPS. *Mon. Wea. Rev.,* **121,** 2373–2395.

Junker, N. W., J. E. Hoke, and R. H. Grumm, 1989: Performance of NMC's regional models. *Wea. Forecasting,* **4,** 368–390.

Kain, J. S., and J. M. Fritsch, 1993: Convective parameterization for mesoscale models: The Kain–Fritsch scheme. *The Representation of Cumulus Convection in Numerical Models, Meteor. Monogr,* No. 46, Amer. Meteor. Soc., 165–170.

Kalnay, E., and Coauthors, 1996: The NCEP/NCAR 40-Year Reanalysis Project. *Bull. Amer. Meteor. Soc.,* **77,** 437–471.

Louis, J. F., M. Tiedtke, and J. F. Geleyn, 1982: A short history of the operational PBL parameterization at ECMWF. *Proc. European Centre for Medium-Range Weather Forecasts Workshop on Planetary Boundary Parameterization,* Reading, United Kingdom, ECMWF, 59–79.

Palmer, T. N., G. J. Shutts, and R. Swinbank, 1986: Alleviation of a systematic westerly bias in general circulation and numerical weather prediction models through an orographic gravity wave drag parameterization. *Quart. J. Roy. Meteor. Soc.,* **112,** 1001–1039.

Reynolds, R. W., and T. M. Smith, 1994: Improved global sea surface temperature analysis using optimum interpolation. *J. Climate,* **7,** 929–948.

Rosmond, T. E., 1992: The design and testing of the Navy Operational Global Atmospheric Prediction System. *Wea. Forecasting,* **7,** 262–272.

Rutledge, S. A., and P. V. Hobbs, 1983: The mesoscale and microscale structure and organization of clouds and precipitation in midlatitude cyclones. VIII: A model for the ''seeder-feeder'' process in warm-frontal rainbands. *J. Atmos. Sci.,* **40,** 1185–1206.

Schubert, S., R. Rood, and J. Pfaendtner, 1993: An assimilated dataset for earth sciences applications. *Bull. Amer. Meteor. Soc.,* **74,** 2331–2342.

Sherman, C. A., 1978: A mass-consistent model for wind fields over complex terrain. *J. Appl. Meteor.,* **17,** 319–321.

Sykes, R. I., W. S. Lewellen, and S. F. Parker, 1984: A turbulent-transport model for concentration fluctuations and fluxes. *J. Fluid. Mech.,* **139,** 193–218.

Tiedtke, M., 1984: The sensitivity of the time-scale flow to cumulus convection in the ECMWF model. *European Centre for Medium-Range Weather Forecasts Workshop on Convection in Large-Scale Numerical Models,* Reading, United Kingdom, ECMWF, 297–316.

Toon, O. B., R. P. Turco, D. L. Westphal, R. Malone, and M. S. Liu, 1988: A multidimensional model for aerosols: Description of computational analogs. *J. Atmos. Sci.,* **45,** 2123–2143.